Theory of third-order spectroscopic methods to extract detailed molecular orientational dynamics for planar surfaces and other uniaxial systems

Jun Nishida and Michael D. Fayer[a)]
Department of Chemistry, Stanford University, Stanford, California 94305, USA

(Received 24 January 2014; accepted 25 March 2014; published online 10 April 2014)

Functionalized organic monolayers deposited on planar two-dimensional surfaces are important systems for studying ultrafast orientational motions and structures of interfacial molecules. Several studies have successfully observed the orientational relaxation of functionalized monolayers by fluorescence depolarization experiments and recently by polarization-resolved heterodyne detected vibrational transient grating (HDTG) experiments. In this article we provide a model-independent theory to extract orientational correlation functions unique to interfacial molecules and other uniaxial systems based on polarization-resolved resonant third-order spectroscopies, such as pump-probe spectroscopy, HDTG spectroscopy, and fluorescence depolarization experiment. It will be shown (in the small beam-crossing angle limit) that five measurements are necessary to completely characterize the monolayer's motions: $I_{\parallel}(t)$ and $I_{\perp}(t)$ with the incident beams normal to the surface, $I_{\parallel}(t)$ and $I_{\perp}(t)$ with a non-zero incident angle, and a time averaged linear dichroism measurement. Once these measurements are performed, two orientational correlation functions corresponding to in-plane and out-of-plane motions are obtained. The procedure is applicable not only for monolayers on flat surfaces, but any samples with uniaxial symmetry such as uniaxial liquid crystals and aligned planar bilayers. The theory is valid regardless of the nature of the actual molecular motions on interface. We then apply the general results to wobbling-in-a-cone model, in which molecular motions are restricted to a limited range of angles. Within the context of the model, the cone angle, the tilt of the cone relative to the surface normal, and the orientational diffusion constant can be determined. The results are extended to describe analysis of experiments where the beams are not crossing in the small angle limit. © *2014 AIP Publishing LLC*. [http://dx.doi.org/10.1063/1.4870436]

I. INTRODUCTION

The properties of molecules on interfaces are of increasing interest, particularly due to recent developments in chemical methodologies used to functionalize various types of surfaces.[1] For example, functionalized surfaces have potential applications as molecular heterogeneous catalysts,[2] and organic molecular coatings can be used to modify surface properties that are useful in biomedical applications.[3] For molecular monolayers bound to a surface, it is useful to determine both the static structure and dynamics of the surface bound molecules. A functional group bound to a surface by alkyl chains will have some average angle relative to the surface normal, as defined by some aspect of the group such as a transition dipole, as well as a distribution of angles (a cone of angles) about the average. In addition, the angles within the cone are not static. Thermal fluctuations will cause the angles to fluctuate. The system will evolve over time such that a range of angles is sampled. This type of orientational dynamics is frequently referred to as wobbling-in-a-cone motion.[4–6] It is of primary interest to elucidate these orientational dynamics of interfacial molecules using time-resolved spectroscopy.

For systems that are isotropic in three dimensions, it is well known how to measure the orientational dynamics using various types of polarized spectroscopies, such as fluorescence depolarization,[7] polarized pump-probe experiments,[8] and polarized transient grating experiments.[9] In experiments with isotropic samples, the anisotropy $r(t)$ is obtained through

$$r(t) = \frac{I_{\parallel}(t) - I_{\perp}(t)}{I_{\parallel}(t) + 2I_{\perp}(t)}, \tag{1.1}$$

where $I_{\parallel}(t)$ is the time dependent signal observed with the excitation and the detection polarizations parallel to each other, and $I_{\perp}(t)$ is the signal with orthogonal polarizations. For isotropic samples, the anisotropy $r(t)$ is directly proportional to the orientational correlation function of the transition dipole moments, $\langle P_2(\hat{\mu}(t) \cdot \hat{\mu}(0))\rangle$, where P_2 is the 2nd order Legendre polynomial.[7,10]

The simplest case is molecules in an isotropic liquid, where the decay of the orientational anisotropy is directly related to the orientational diffusion constant.[7] It is also known how to treat molecules at interfaces if the interfaces supporting the molecules are randomly oriented in the sample. Examples of such systems are fluorophores adsorbed on surfaces of an ensemble of randomly oriented porous silica particles,[11,12] fluorophores embedded in randomly oriented bilayers,[13] and water molecules at the interface of reverse micelles.[14,15] In such systems, the orientational relaxation of the chromophore under observation may not sample all angles. However, as long as the initial distribution of transition dipole directions is isotropic, the anisotropy given in Eq. (1.1) is still directly proportional to orientational correlation function. The anisotropy,

a)fayer@stanford.edu

$r(t)$, measured for these surface bound molecules in a system with overall random orientation typically shows a decay followed by a significant plateau. The wobbling-in-a-cone theory[4–6,16] relates the decay time constant and the plateau level to the cone angle (angular width of the cone) and the orientational diffusion constant. The cone angle is extracted from the plateau level observed in $r(t)$. Combining the cone angle and the $r(t)$ decay constant yields the angular diffusion constant for motion in the cone of angles. With this theoretical framework, time-resolved depolarization spectroscopies have been useful in providing a detailed picture of interfacial molecular motions for 3D isotropic systems.

While the approach outlined above for investigating static angular distributions and the dynamics of surface bound molecules provides useful information, it has limitations. Experiments on dispersed isotropic 3D systems cannot address the questions of (1) how the interfacial molecules are oriented relative to the surface (the tilt angle of the cone relative to the surface normal) and (2) how in-plane and out-of-plane orientational dynamics differ.

To extract these structural and dynamical properties unique to interfaces, the polarization-resolved measurements must be applied to molecules bound to or at two-dimensional (flat) surfaces. There are numerous reports of static (time averaged) molecular orientations on surfaces and in membranes studied by fluorescence and IR linear dichroism spectroscopic methods.[17–24] Sum-frequency generation (SFG) spectroscopy has also provided detailed structural information for molecules at liquid-air interfaces.[25] Compared with these static properties, the studies of orientational dynamics of molecules on two-dimensional interfaces are limited. Polarization-resolved pump-probe SFG spectroscopies have been applied to observe the orientational relaxation of molecules on liquid-air interfaces.[26–29] Also, fluorescence probes were introduced selectively at liquid-liquid or liquid-air interfaces to study their reorientation dynamics by time-resolved fluorescence depolarization spectroscopy.[30–32] Most recently, an organic monolayer functionalized with a vibrational probe was studied, and the results demonstrated that picosecond orientational motions of the monolayer can be probed by polarization-resolved infrared heterodyne detected transient grating (HDTG) spectroscopy.[33]

These studies were successful in providing some important insights about the in-plane and out-of-plane motions of interfacial molecules, although the interpretations involved model dependent assumptions. It is generally assumed that in-plane and out-of-plane motions of interfacial molecules are decoupled.[26,30] This assumption is not valid in general as seen in examples shown in Sec. III. A model independent theory to extract in-plane and out-of-plane orientational motions is required.

Zannoni[34] and Szabo[35] independently studied the fluorescence depolarization of probes in thick samples of macroscopically aligned uniaxial liquid crystals in a model independent manners. In these studies it was pointed out that the anisotropy in Eq. (1.1) is not directly proportional to the orientational correlation function for uniaxial systems, but there is still a linear relationship for the case in which the polarization (E-field) of the excitation beam is set parallel to the C_∞ symmetry axis of liquid crystal. Molecules on a planar interface, such as an organic monolayer, can be regarded as a uniaxial system where the normal to the substrate's surface is the C_∞ axis. To apply the theories by Zannoni and Szabo to the case of two-dimensional monolayers, the excitation beam must propagate virtually parallel to the surface with a grazing angle so that the polarization of the excitation beam is normal to the surface. This geometry was previously used for fluorescence experiment to probe out-of-plane motions of interfacial molecules,[30–32] but is impractical for many of the spectroscopic methods, such as HDTG and pump-probe spectroscopies. Furthermore, in this approach only the out-of-plane motions can be studied; a model independent method for probing the in-plane motion of molecules has not been presented.

In this article, we present a model independent theory to fully characterize dynamical and structural properties of interfacial molecules on a two-dimensional surface (flat surface) based on third-order resonant spectroscopies, such as fluorescence depolarization spectroscopy, polarization-resolved pump-probe spectroscopy, and polarization-resolved HDTG spectroscopy. It will be also shown that the theory is valid for any system with uniaxial symmetry. The discussion will proceed in the following manner. In Sec. II, we will first show that the necessary response functions can be rigorously expressed in terms of the following four quantities: the time dependent correlation functions of spherical harmonics ($\langle Y_2^{0*} Y_2^0 \rangle$ and $\langle Y_2^{2*} Y_2^2 \rangle$), a parameter reflecting time average of molecular orientation ($\langle Y_2^0 \rangle$), and a time dependent isotropic population decay ($P(t)$). Based on the formulas obtained for the response functions, we prove that these four terms can be experimentally obtained by the four measurements: $I_\parallel(t)$ and $I_\perp(t)$ with the beam(s) incident normal to the surface, $I_\perp(t)$ with a certain incident angle χ (tilted surface), and also the time averaged fluorescence or infrared linear dichroism. In an actual experiment, $I_\parallel(t)$ with the same incident angle χ is also necessary to account for the difference in the number of molecules in the focal volume between the two different surface configurations. The anisotropy $r(t)$ given by Eq. (1.1) is not the correct quantity to extract the dynamical and structural information. Instead, the spherical harmonic correlations functions, $\langle Y_2^{0*} Y_2^0 \rangle$ and $\langle Y_2^{2*} Y_2^2 \rangle$, are the set of orientational correlation functions.

In Sec. III, model calculation from the response functions derived in Sec. II is presented for molecules (transition dipole moments) displaying wobbling-in-a-cone motions on a planar surface. It is shown how the cone angle (width of the cone) and the cone tilt angle (angle the cone axis makes with the normal) affect the response functions. In Sec. IV the procedure to extract the orientational correlation functions from two test cases is presented. In Secs. II–IV, it is assumed that the crossing angles between the beams are infinitely small. In real experiments non-negligible crossing angles may be necessary to separate the excitation beams from the signal or to collect a measurable amount of fluorescence. The detailed expressions for the response functions for various beam geometries and crossing angles are presented in Sec. V with their derivations given in the supplementary material.[36]

II. GENERAL EXPRESSIONS FOR RESPONSE FUNCTIONS

In this section, we will derive the model-independent formulas for the response functions in terms of averages and time correlation functions of spherical harmonics. The well-established method to express the response functions with dipole interactions and Green's functions is briefly reviewed in Sec. II A. In Sec. II B the advantage of expressing the interactions in the "surface frame" (S) is discussed. The response functions for the simplest case are calculated as a demonstration. Following the procedures discussed in Secs. II A and II B, the response functions for several cases are calculated in Sec. II C. The experimental procedure to fully characterize molecular motions is also given in Sec. II C.

Throughout this paper, it will be assumed that excitation transition dipole moment and the transition dipole moment used for the observation step are identical. The assumption is met for pump-probe experiments and transient grating experiments in which the same transition is excited and probed. However, it is not always true for fluorescence experiments.[5,35] The theory as presented is applicable to fluorescence probes with the same excitation and emission transition dipoles.

A. Response functions and dipole interactions

In third-order resonant nonlinear spectroscopy, the third-order nonlinear polarization induced by three incident electric fields generates the signal, which can be expressed by[37,38]

$$P_{\eta}^{(3)}(t) = (-i)^3 \int_0^{\infty} dt_3 \int_0^{\infty} dt_2 \int_0^{\infty} dt_1 \times R_{\eta\gamma\beta\alpha}^{(3)}(t_3, t_2, t_1) \exp[i(\omega_3 + \omega_2 + \omega_1)t_3 + i(\omega_2 + \omega_1)t_2 + i\omega_1 t_1] \times E_{3,\gamma}(t - t_3) E_{2,\beta}(t - t_2 - t_3) E_{1,\alpha}(t - t_1 - t_2 - t_3). \tag{2.1}$$

Equation (2.1) is the time-domain representation of the nonlinear polarization oscillating at $\omega = \omega_1 + \omega_2 + \omega_3$, where ω_i is a frequency of the ith input E-field. A sequence of three E-fields interacts with the matter in the order of E_1, E_2, and E_3. The three fields occur with the intervals of t_1 and t_2, and the polarization created is monitored after time t_3 from the last input interaction. $R^{(3)}$ is the third-order response function, which is a function of time-intervals and polarizations of the incident E-fields. This representation is useful for time-resolved experiment. Here, we limit our discussion to the cases of pump-probe experiment or heterodyne detected transient grating (HDTG) experiment. In these cases, t_1 and t_3 can be set to 0 with $\omega_2 = -\omega_1$, because the first two interactions occur simultaneously and the resultant signal is emitted as soon as the third interaction with the transition dipole occurs.[10] The pulses are taken to be delta functions in time. The method to include the effect of finite pulse duration is well known,[39] but frequently unnecessary. For delta function E-fields, Eq. (2.1) reduces to

$$P_{\eta}^{(3)}(t) = (-i)^3 R_{\eta\gamma\beta\alpha}^{(3)}(0, t_2, 0) E_{3,\gamma} E_{2,\beta}^{*} E_{1,\alpha}. \tag{2.2}$$

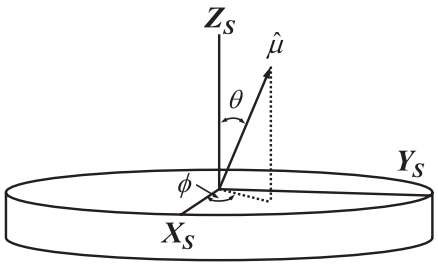

FIG. 1. Illustration of the surface frame (X_S, Y_S, Z_S). The $X_S Y_S$ plane is in the plane of the surface, while Z_S axis is normal to the surface. The direction of each transition dipole $\hat{\mu}$ is described by polar angle θ and azimuthal angle ϕ.

Thus the direct observable in these experiments is the response function $R_{\eta\gamma\beta\alpha}^{(3)}(0, t_2, 0)$. In the following discussion, this response function $R_{\eta\gamma\beta\alpha}^{(3)}(0, t_2, 0)$ is denoted as $R_{\eta\gamma\beta\alpha}^{\text{tot}}(t)$, where t is used instead of t_2 to represent the interval between the first two instantaneous interactions and the third interaction.

The total response function $R_{\eta\gamma\beta\alpha}^{\text{tot}}(t)$ is separated into the orientational response function $R_{\eta\gamma\beta\alpha}(t)$ and the isotropic population decay (relaxation to the ground electronic or vibrational state) $P(t)$:

$$R_{\eta\gamma\beta\alpha}^{\text{tot}}(t) = R_{\eta\gamma\beta\alpha}(t) \times P(t). \tag{2.3}$$

Our interest is how the orientational response function $R_{\eta\gamma\beta\alpha}(t)$ is related to the motion of a transition dipole moment on a molecule bound to a planar surface.

The molecular orientational motion is described by the time-dependence of the direction of the transition dipole moment specified by polar angle θ and azimuthal angle ϕ in the surface frame (S) as illustrated in Figure 1. Here we consider $G'(\Omega_1, t|\Omega_0)$, which is the probability that a transition dipole oriented at $\Omega_0 = (\theta_0, \phi_0)$ at $t = 0$ is oriented at $\Omega_1 = (\theta_1, \phi_1)$ after time t. For the ensemble of molecules bound to the surface, the equilibrated distribution of transition dipole orientations is $P_{\text{eq}}(\Omega)$. By defining Green's function $G(\Omega_1, t|\Omega_0)$ as

$$G(\Omega_1, t|\Omega_0) = G'(\Omega_1, t|\Omega_0) P_{\text{eq}}(\Omega_0), \tag{2.4}$$

the orientational response function can be written as

$$R_{\eta\gamma\beta\alpha}(t) = \int d\Omega_1 \int d\Omega_0 (\hat{\mu}_1 \hat{\varepsilon}_\eta)(\hat{\mu}_1 \hat{\varepsilon}_\gamma) G(\Omega_1, t|\Omega_0) \times (\hat{\mu}_0 \hat{\varepsilon}_\beta)(\hat{\mu}_0 \hat{\varepsilon}_\alpha), \tag{2.5}$$

where $\hat{\mu}_i$ is a unit vector pointing the direction of $\Omega_i = (\theta_i, \phi_i)$, $\hat{\varepsilon}_\alpha$, $\hat{\varepsilon}_\beta \cdots$ is a unit vector parallel to incident E-field with α, $\beta \cdots$ polarizations. The meaning of Eq. (2.5) can be intuitively understood in the following manner. A transition dipole moment oriented with angles Ω_0 interacts instantaneously with α and β polarized E-fields. This transition dipole undergoes reorientation to the direction Ω_1 with the probability $G(\Omega_1, t|\Omega_0)$, then interacts with a γ polarized E-field after time t, and at the same time t emits an η polarized signal.

The central topic of this paper is the calculation of Eq. (2.5) for a two-dimensional monolayer on a planar surface with various sets of incident polarizations and beam

geometries. It is worth mentioning that Eq. (2.5) is applicable to fluorescence depolarization experiments as well as pump-probe and transient grating experiments. In the semi-classical response function method, absorption or emission of a photon corresponds to two E-field interactions; because fluorescence is generated by absorption of one photon followed by emission of one photon, Eq. (2.5) is valid for fluorescence depolarization experiments as well.[7] Thus time resolved fluorescence depolarization can be treated as a third-order spectroscopy.

B. Dipole interactions and corresponding spherical harmonics representations

Since our interest is in the dynamics of a transition dipole in the surface frame (S), it is convenient to describe all interactions associated with Eq. (2.5) in the S. For this purpose, the polarizations of incident E-fields $\hat{\varepsilon}_\alpha$, $\hat{\varepsilon}_\beta \cdots$ given in the lab frame (L) are converted to the S. This transformation depends on the experimental configuration. In the simplest case where the surface is normal to the propagation direction of the beam (Figure 2(a)), L and S can be simply set so that

$$\hat{\varepsilon}_{X_L} = \hat{\varepsilon}_{X_S}, \tag{2.6}$$

$$\hat{\varepsilon}_{Y_L} = \hat{\varepsilon}_{Y_S}. \tag{2.7}$$

If the beam is incident on the surface with finite incident angle χ (Figure 2(b)), the transformation between L and S is given by

$$\hat{\varepsilon}_{X_L} = \hat{\varepsilon}_{X_S}, \tag{2.8}$$

$$\hat{\varepsilon}_{Y_L} = \cos\chi \cdot \hat{\varepsilon}_{Y_S} + \sin\chi \cdot \hat{\varepsilon}_{Z_S}. \tag{2.9}$$

Once the E-fields are expressed in the S, all the quantities in Eq. (2.5) can be expressed in terms of Ω_0 and Ω_1.

As a demonstration, consider the case in which all of the incident and output polarizations are X_L-polarized in the L, and the surface is set normal to the propagation direction of the beam ($\chi = 0^\circ$; Figure 2(a)). For the beams impinging on the surface with no crossing angle, the corresponding orientational response function is

$$\begin{aligned} R^{\chi=0^\circ}_{XXXX}(t) &= \int d\Omega_1 \int d\Omega_0 (\hat{\mu}_1 \hat{\varepsilon}_{X_L})^2 G(\Omega_1, t\,|\,\Omega_0)(\hat{\mu}_0 \hat{\varepsilon}_{X_L})^2 \\ &= \int d\Omega_1 \int d\Omega_0 (\hat{\mu}_1 \hat{\varepsilon}_{X_S})^2 G(\Omega_1, t\,|\,\Omega_0)(\hat{\mu}_0 \hat{\varepsilon}_{X_S})^2. \end{aligned} \tag{2.10}$$

Here, $\hat{\mu}_i \hat{\varepsilon}_{X_S} = \sin\theta_i \cos\phi_i$ in the S and thus $(\hat{\mu}_i \hat{\varepsilon}_{X_S})^2 = \sin^2\theta_i \cos^2\phi_i$. Using the definitions of the spherical harmonics,[10,40]

$$Y_2^0(\theta,\phi) = \frac{1}{4}\sqrt{\frac{5}{\pi}}(3\cos^2\theta - 1), \tag{2.11}$$

$$Y_2^{\pm 2}(\theta,\phi) = \frac{1}{4}\sqrt{\frac{15}{2\pi}}\sin^2\theta e^{\pm 2i\phi}. \tag{2.12}$$

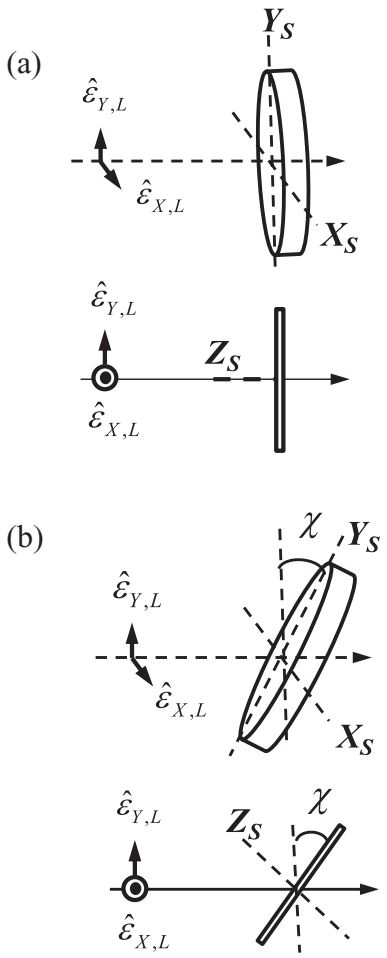

FIG. 2. Two experimental configurations discussed in Sec. II in the small crossing angle limit, i.e., all the incident beams have the same k-vector. The polarization of the incident beams are either $\hat{\varepsilon}_{X,L}$ or $\hat{\varepsilon}_{Y,L}$ in lab frame. (a) The surface is normal to the k-vectors of the incident beams. The surface frame can be defined so that X_S axis and Y_S axis are parallel to $\hat{\varepsilon}_{X,L}$ and $\hat{\varepsilon}_{Y,L}$ respectively. By definition, Z_S axis is along the k-vectors of the incident beams. (b) The surface is tilted by angle χ so that $\hat{\varepsilon}_{Y,L}$ is no longer parallel to the Y_S axis, while $\hat{\varepsilon}_{X,L}$ is still parallel to the X_S axis. The Z_S axis makes the angle χ relative to the k-vectors of the incident beams.

$(\hat{\mu}_i \hat{\varepsilon}_{X_S})^2 = \sin^2\theta_i \cos^2\phi_i$ can be re-expressed as

$$(\hat{\mu}_i \hat{\varepsilon}_{X_S})^2 = \frac{1}{3} - \frac{2}{3}\sqrt{\frac{\pi}{5}}Y_2^0(\Omega_i) + \sqrt{\frac{2\pi}{15}}\left[Y_2^2(\Omega_i) + Y_2^{-2}(\Omega_i)\right]. \tag{2.13}$$

Equation (2.13) is substituted into Eq. (2.10) to yield

$$\begin{aligned} &R^{\chi=0^\circ}_{XXXX}(t) \\ &= \int d\Omega_1 \int d\Omega_0 \left[\frac{1}{3} - \frac{2}{3}\sqrt{\frac{\pi}{5}}Y_2^0(\Omega_1) \right. \\ &\quad \left. + \sqrt{\frac{2\pi}{15}}\left\{Y_2^2(\Omega_1) + Y_2^{-2}(\Omega_1)\right\}\right] G(\Omega_1, t\,|\,\Omega_0) \\ &\quad \times \left[\frac{1}{3} - \frac{2}{3}\sqrt{\frac{\pi}{5}}Y_2^0(\Omega_0) + \sqrt{\frac{2\pi}{15}}\left\{Y_2^2(\Omega_0) + Y_2^{-2}(\Omega_0)\right\}\right]. \end{aligned} \tag{2.14}$$

TABLE I. Matter-*E*-field dipole interactions arising from the evaluation of Eq. (2.5), and corresponding trigonometric functions and spherical harmonics representations. Note that the subscript *S* indicates the surface frame. The incident *E*-fields in lab frame must be transformed to the surface frame.

Dipole interactions	Trigonometric functions representation	Spherical harmonics representation
$(\hat{\mu}\hat{\varepsilon}_{X,S})^2$	$\sin^2\theta\cos^2\phi$	$\frac{1}{3}-\frac{2}{3}\sqrt{\frac{\pi}{5}}Y_2^0+\sqrt{\frac{2\pi}{15}}(Y_2^2+Y_2^{-2})$
$(\hat{\mu}\hat{\varepsilon}_{Y,S})^2$	$\sin^2\theta\sin^2\phi$	$\frac{1}{3}-\frac{2}{3}\sqrt{\frac{\pi}{5}}Y_2^0-\sqrt{\frac{2\pi}{15}}(Y_2^2+Y_2^{-2})$
$(\hat{\mu}\hat{\varepsilon}_{Z,S})^2$	$\cos^2\theta$	$\frac{1}{3}+\frac{4}{3}\sqrt{\frac{\pi}{5}}Y_2^0$
$(\hat{\mu}\hat{\varepsilon}_{X,S})(\hat{\mu}\hat{\varepsilon}_{Y,S})$	$\sin^2\theta\sin\phi\cos\phi$	$-i\sqrt{\frac{2\pi}{15}}(Y_2^2-Y_2^{-2})$
$(\hat{\mu}\hat{\varepsilon}_{Z,S})(\hat{\mu}\hat{\varepsilon}_{X,S})$	$\sin\theta\cos\theta\cos\phi$	$-\sqrt{\frac{2\pi}{15}}(Y_2^1-Y_2^{-1})$
$(\hat{\mu}\hat{\varepsilon}_{Z,S})(\hat{\mu}\hat{\varepsilon}_{Y,S})$	$\sin\theta\cos\theta\sin\phi$	$i\sqrt{\frac{2\pi}{15}}(Y_2^1+Y_2^{-1})$

By expanding Eq. (2.14), $R_{XXXX}^{\chi=0^\circ}(t)$ can be expressed in terms of the following time-correlation function (Eq. (2.15)) and the time-average (Eq. (2.16)) of the spherical harmonics:

$$\begin{aligned}\left\langle Y_2^{m^*}Y_2^{m'}\right\rangle &\equiv \left\langle Y_2^{m^*}(t)Y_2^{m'}(0)\right\rangle \\ &\equiv \int d\Omega_1\int d\Omega_0 Y_2^{m^*}(\Omega_1)G(\Omega_1,t|\,\Omega_0)Y_2^{m'}(\Omega_0),\end{aligned} \tag{2.15}$$

$$\begin{aligned}\left\langle Y_2^{m}\right\rangle &\equiv \int d\Omega_1\int d\Omega_0 Y_2^{m}(\Omega_1)G(\Omega_1,t|\,\Omega_0) \\ &= \int d\Omega_1\int d\Omega_0 G(\Omega_1,t|\,\Omega_0)Y_2^{m}(\Omega_0).\end{aligned} \tag{2.16}$$

$Y_2^{m^*}$ denotes the complex conjugate of Y_2^m. It can be rigorously proven that a system which is macroscopically symmetric in-plane, regardless of the actual functional form of $G(\Omega_1, t|\Omega_0)$, obeys the following orthogonality relations for the correlation function of the spherical harmonics.

$$\left\langle Y_2^{m^*}Y_2^{m'}\right\rangle \propto \delta_{mm'}, \tag{2.17}$$

$$\left\langle Y_2^{m}\right\rangle \propto \delta_{m0}. \tag{2.18}$$

The derivations of Eqs. (2.17) and (2.18) are given in Section A of the supplementary material.[36] It is reasonable to assume that a functionalized monolayer does not have macroscopic directionality. The orthogonality relations given in Eqs. (2.17) and (2.18) greatly simplify the expansion of Eq. (2.14) to yield

$$R_{XXXX}^{\chi=0^\circ}(t)=\frac{1}{9}-\frac{4}{9}\sqrt{\frac{\pi}{5}}\left\langle Y_2^0\right\rangle+\frac{4}{45}\pi\left\langle Y_2^{0^*}Y_2^0\right\rangle+\frac{4}{15}\pi\left\langle Y_2^{2^*}Y_2^2\right\rangle. \tag{2.19}$$

In the derivation of Eq. (2.19), the relations $Y_2^{2^*}=Y_2^{-2}$, $Y_2^{0^*}=Y_2^0$ and $\langle Y_2^{2^*}Y_2^2\rangle=\langle Y_2^{-2^*}Y_2^{-2}\rangle$ were used. Note that as seen in Eqs. (2.15) and (2.16), $\langle Y_2^0\rangle$ is time independent while $\langle Y_2^{0^*}Y_2^0\rangle\equiv\langle Y_2^{0^*}(t)Y_2^0(0)\rangle$ and $\langle Y_2^{2^*}Y_2^2\rangle\equiv\langle Y_2^{2^*}(t)Y_2^2(0)\rangle$ are time dependent. Thus the orientational response function can be expressed in terms of the time independent average and the time dependent correlation functions of spherical harmonics in the surface frame.

The same procedure can be followed to calculate response functions with other sets of input polarizations. All the necessary matter-*E*-field transition dipole interactions and corresponding representations with spherical harmonics are given in Table I. To summarize, the response functions are represented using the Green's function and the polarizations of the *E*-fields in the surface frame (Eq. (2.10)). Then the dipole interactions are replaced by their spherical harmonics representations in Table I (Eq. (2.14)). The expansion of the representation in terms of correlation functions and average of spherical harmonics, with the use of orthogonality of the spherical harmonics, will lead to equivalent of Eq. (2.19).

C. Derivations of orientational correlation functions from response functions

We first consider implementing the polarization-resolved pump-probe experiment with the most natural configuration shown in Figure 2(a), where the propagation direction of the incident beams is normal to the surface. The sample is assumed to be a molecular monolayer on a solid planar surface. Here the crossing angle between the pump and probe beams is zero. Finite crossing angles are discussed in Sec. V and the supplementary material.[36] For some situations, the zero crossing angle results are applicable without modifications even with finite crossing angles. The polarization of the pump beam is always set to either X_L or Y_L, whereas the polarization for the probe beam is always fixed to X_L. The observed signals are the response functions $R_{XXXX}^{\chi=0^\circ}(t)$ (pump and probe polarizations parallel) and $R_{XXYY}^{\chi=0^\circ}(t)$ (pump and probe polarizations perpendicular). As discussed in Sec. II A, the response functions are factored into orientational correlation functions and an isotropic population decay. The orientational correlation function for $R_{XXXX}^{\chi=0^\circ}(t)$ was obtained in Sec. II B, Eq. (2.19). In the same manner, the orientational correlation function for $R_{XXYY}^{\chi=0^\circ}(t)$ can be calculated by evaluating

$$R_{XXYY}^{\chi=0^\circ}(t)=\int d\Omega_1\int d\Omega_0(\hat{\mu}_1\hat{\varepsilon}_{X,S})^2G(\Omega_1,t|\,\Omega_0)(\hat{\mu}_0\hat{\varepsilon}_{Y,S})^2. \tag{2.20}$$

Including the isotropic population decay, the response functions as observables can be written as

$$R^{\chi=0^\circ}_{XXXX}(t) = \left[\frac{1}{9} - \frac{4}{9}\sqrt{\frac{\pi}{5}}\langle Y_2^0\rangle + \frac{4}{45}\pi\langle Y_2^{0^*}Y_2^0\rangle + \frac{4}{15}\pi\langle Y_2^{2^*}Y_2^2\rangle\right] \times P(t), \quad (2.21)$$

$$R^{\chi=0^\circ}_{XXYY}(t) = \left[\frac{1}{9} - \frac{4}{9}\sqrt{\frac{\pi}{5}}\langle Y_2^0\rangle + \frac{4}{45}\pi\langle Y_2^{0^*}Y_2^0\rangle - \frac{4}{15}\pi\langle Y_2^{2^*}Y_2^2\rangle\right] \times P(t). \quad (2.22)$$

The physical meanings of Eqs. (2.21) and (2.22) can be seen when the original forms of the spherical harmonics, Eq. (2.11) and (2.12), are referred to. Y_2^0 only depends on polar angle θ, thus $\langle Y_2^0\rangle$ reflects average polar angle of transition dipole moments, and $\langle Y_2^{0^*}Y_2^0\rangle$ corresponds to out-of-plane motion of the transition dipoles. On the other hand, Y_2^2 contains both polar angle θ and azimuthal angle ϕ. Y_2^2 is directly proportional to $e^{\pm 2i\phi}$. Considering that the polar motions of organic molecules bound to a surface are generally restricted, $\langle Y_2^{2^*}Y_2^2\rangle$ can be interpreted as mainly in-plane motions coupled to some extent of out-of-plane motions. Because the polarizations of the E-fields are in-plane in the experimental configuration shown in Figure 2(a), the in-plane motions will contribute differently to the two response functions, while the contribution from out-of-plane motion should be the same, which can be seen in Eqs. (2.21) and (2.22). $\langle Y_2^{0^*}Y_2^0\rangle$ contributes to the response functions with the positive sign in both equations, while the signs for the $\langle Y_2^{2^*}Y_2^2\rangle$ terms are opposite.

These response functions in Eqs. (2.21) and (2.22) are in contrast to the response functions for randomly orientated transition dipoles in isotropic (iso) 3D space in terms of the number of unknown variables. These are given by[7,10]

$$R^{\rm iso}_{XXXX}(t) = \frac{1}{9}\left\{1 + \frac{4}{5}c_2(t)\right\}P(t), \quad (2.23)$$

$$R^{\rm iso}_{XXYY}(t) = \frac{1}{9}\left\{1 - \frac{2}{5}c_2(t)\right\}P(t). \quad (2.24)$$

$c_2(t)$ is orientational correlation function $\langle P_2(\hat{\mu}(t)\cdot\hat{\mu}(0))\rangle$, where P_2 is the second-order Legendre polynomial. As is clear from Eqs. (2.23) and (2.24), $R^{\rm iso}_{XXXX}(t)$ and $R^{\rm iso}_{XXYY}(t)$ contain only two time dependent parameters $c_2(t)$ and $P(t)$. Thus, the measurements of the two observables described by Eqs. (2.23) and (2.24) are sufficient to obtain both of the unknown parameters, $c_2(t)$ and $P(t)$ using the standard forms,

$$P(t) \propto R^{\rm iso}_{XXXX} + 2R^{\rm iso}_{XXYY}, \quad (2.25)$$

$$\frac{2}{5}c_2(t) = \frac{R^{\rm iso}_{XXXX} - R^{\rm iso}_{XXYY}}{R^{\rm iso}_{XXXX} + 2R^{\rm iso}_{XXYY}} \equiv r(t). \quad (2.26)$$

For the case of a two-dimensional planar monolayer, the response functions in Eqs. (2.21) and (2.22) contain three time dependent parameters ($\langle Y_2^{0^*}Y_2^0\rangle$, $\langle Y_2^{2^*}Y_2^2\rangle$, and $P(t)$) and one time averaged parameter, $\langle Y_2^0\rangle$. Because there are four unknown parameters in total, at least four measurements are necessary to uniquely determine all of these parameters; the two measurements, $R^{\chi=0^\circ}_{XXXX}(t)$ and $R^{\chi=0^\circ}_{XXYY}(t)$, are not sufficient to fully characterize molecular motions on a planar surface. Two other measurements are required.

Among the unknown parameters in Eqs. (2.21) and (2.22), the time averaged parameter, $\langle Y_2^0\rangle = \frac{1}{4}\sqrt{\frac{5}{\pi}}\langle 3\cos^2\theta - 1\rangle$, is directly related to the well-known order parameter[17,18,23,41]

$$\langle S\rangle = \frac{1}{2}\langle 3\cos^2\theta - 1\rangle. \quad (2.27)$$

The order parameter $\langle S\rangle$ can be measured by absorption (visible or IR) or fluorescence linear dichroism experiments. In these static experiments, p and s polarized light (continuous wave) impinge on the surface with a defined incident angle. Based on the incident angle and independently measured absorbance (or fluorescence emission) for p and s polarized light, the order parameter $\langle S\rangle$ can be obtained. The details for these experiments are found in literature.[41] Once these measurements are made and $\langle S\rangle$ is experimentally determined, $\langle Y_2^0\rangle$ is obtained as

$$\langle Y_2^0\rangle = \frac{1}{2}\sqrt{\frac{5}{\pi}}\langle S\rangle. \quad (2.28)$$

We still need another measurement to complete the determination of the four unknown parameters. The necessary additional measurement can be made with a time-resolved polarization-resolved pump-probe experiment using the configuration shown in Figure 2(b). In Figure 2(b), the surface is tilted so that Y_L-polarization in lab frame makes angle χ with the surface. Again the pump polarization is set to either X_L or Y_L (lab frame), while the probe polarization is fixed to X_L. The observed signals for each set of polarizations are denoted by $R^{\chi}_{XXXX}(t)$ and $R^{\chi}_{XXYY}(t)$. Since X_L polarization is insensitive to the difference in configurations between Figures 2(a) and 2(b),

$$R^{\chi}_{XXXX}(t) = R^{\chi=0^\circ}_{XXXX}(t) \quad (2.29)$$

Unlike $R^{\chi}_{XXXX}(t)$, $R^{\chi}_{XXYY}(t)$ is not equal to $R^{\chi=0^\circ}_{XXYY}(t)$. Following the transformation of E-fields between the lab frame and the surface frame given in Eqs. (2.8) and (2.9),

$$R^{\chi}_{XXYY}(t) = \int d\Omega_1 \int d\Omega_0 (\hat{\mu}_1\hat{\varepsilon}_{X,S})^2 G(\Omega_1, t|\,\Omega_0) \times \{(\cos\chi\cdot\hat{\mu}_0\hat{\varepsilon}_{Y,S} + \sin\chi\cdot\hat{\mu}_0\hat{\varepsilon}_{Z,S})\}^2. \quad (2.30)$$

Equation (2.30) again can be expanded and expressed in terms of spherical harmonics using Table I. The orthogonality of spherical harmonics, Eqs. (2.17) and (2.18), is very useful to simplify the representation; the result is

$$R^{\chi}_{XXYY}(t) = \left[\frac{1}{9} - \frac{2}{9}\sqrt{\frac{\pi}{5}}(3\cos^2\chi - 1)\langle Y_2^0\rangle + \frac{4\pi}{45}(3\cos^2\chi - 2)\langle Y_2^{0^*}Y_2^0\rangle - \frac{4\pi}{15}\cos^2\chi\langle Y_2^{2^*}Y_2^2\rangle\right] \times P(t). \quad (2.31)$$

Note that by substituting $\chi = 0^\circ$ into Eq. (2.31), Eq. (2.22) is correctly recovered.

Now that there are four independent observables containing four unknown parameters, all of the four parameters, $\langle Y_2^0 \rangle$, $\langle Y_2^{0^*} Y_2^0 \rangle$, $\langle Y_2^{2^*} Y_2^2 \rangle$, and $P(t)$, can be constructed from the observables, $R_{XXXX}^{\chi=0^\circ}(t)$, $R_{XXYY}^{\chi=0^\circ}(t)$, $R_{XXYY}^{\chi}(t)$, and $\langle S \rangle$, by solving Eqs. (2.21), (2.22), (2.28) and (2.31). $R_{XXYY}^{\chi}(t)$ can be measured with any non-zero χ. The solution becomes particularly simple when the angle χ is set so that $\cos^2 \chi = \frac{2}{3}$, i.e., $\chi = 35.3^\circ$. In this case, Eq. (2.31) is reduced to

$$R_{XXYY}^{\chi=35.3^\circ}(t) = \left[\frac{1}{9} - \frac{2}{9}\sqrt{\frac{\pi}{5}} \langle Y_2^0 \rangle - \frac{8\pi}{45} \langle Y_2^{2^*} Y_2^2 \rangle \right] \times P(t). \tag{2.32}$$

By solving Eqs. (2.21), (2.22), (2.28) and (2.32), the time dependent parameters can be obtained:

$$P(t) \propto R_{XXXX}^{\chi=0^\circ}(t) + 3R_{XXYY}^{\chi=35.3^\circ}(t) - R_{XXYY}^{\chi=0^\circ}(t), \tag{2.33}$$

$$\langle Y_2^{2^*} Y_2^2 \rangle = \frac{5}{8\pi} (1 - \langle S \rangle) \cdot \frac{R_{XXXX}^{\chi=0^\circ}(t) - R_{XXYY}^{\chi=0^\circ}(t)}{R_{XXXX}^{\chi=0^\circ}(t) + 3R_{XXYY}^{\chi=35.3^\circ}(t) - R_{XXYY}^{\chi=0^\circ}(t)}, \tag{2.34}$$

$$\langle Y_2^{0^*} Y_2^0 \rangle = \frac{5}{8\pi} \frac{Q(t)}{R_{XXXX}^{\chi=0^\circ}(t) + 3R_{XXYY}^{\chi=35.3^\circ}(t) - R_{XXYY}^{\chi=0^\circ}(t)}, \tag{2.35}$$

where

$$Q(t) = (1 + \langle S \rangle) R_{XXXX}^{\chi=0^\circ}(t) - 6(1 - 2\langle S \rangle) R_{XXYY}^{\chi=35.3^\circ}(t) + (5 - 7\langle S \rangle) R_{XXYY}^{\chi=0^\circ}(t). \tag{2.36}$$

Equations (2.33)–(2.35) are important results stating that the pure population decay $P(t)$, the in-plane motion $\langle Y_2^{2^*} Y_2^2 \rangle$, and the out-of-plane motion $\langle Y_2^{0^*} Y_2^0 \rangle$ can be directly and independently obtained by the three time dependent measurements together with the time averaged linear dichroism experiment.

It should be emphasized that the only assumption we have made so far to derive Eqs. (2.33)–(2.35) is the symmetry of the surface in the plane, which permits the orthogonality of spherical harmonics correlation functions, Eqs. (2.17) and (2.18), to be employed. As long as in-plane symmetry is guaranteed, regardless of the actual functional forms of Green's function, Eqs. (2.21), (2.22) and (2.32) are mathematically rigorous and so are Eqs. (2.33)–(2.35). In the following discussions in Secs. III and IV, it is assumed that the origin of the depolarization is the wobbling-in-a-cone motion of the molecules and their transition dipole moments, but the procedure is completely valid for any other types of motions. The depolarization does not have to originate from motions of molecules but can be induced by Förster excitation transfer as well.[42,43]

In the above discussion, a planar monolayer was considered to derive Eqs. (2.33)–(2.35), but the theory is valid for any system with uniaxial symmetry. For example, the substrate of the monolayer can be rough as long as surface roughness does not have certain directionality in plane. The sample does not have to be a single layer of molecules but can be thick samples such as uniaxial liquid crystals and aligned phospholipid multibilayers. For these thick samples the measurement should be implemented so that Z_S axis in Figure 2 matches C_∞ axis of the samples. Then the correlation function $\langle Y_2^{2^*} Y_2^2 \rangle$ reflects the motion of molecules in the plane perpendicular to the C_∞ axis, while $\langle Y_2^{0^*} Y_2^0 \rangle$ gives the molecular motions out of the plane. Thus the experimental procedure proposed here can provide detailed information on molecular motions in any type of the uniaxial system in contrast to procedures using the anisotropy in Eq. (1.1).[34,35]

It is important to emphasize that to obtain the parameters from Eqs. (2.33)–(2.35), the experimental measurements of $R_{XXXX}^{\chi=0^\circ}(t)$, $R_{XXYY}^{\chi=0^\circ}(t)$ and $R_{XXYY}^{\chi}(t)$ must be made so that their amplitudes are correct. However, when the sample is tilted as shown in Figure 2(b) to make the measurement with $\chi \neq 0$, the number of molecules in the focal volume, the intensity of E-field per surface area, and the reflectivity of the beams from the surface will all change relative to the configuration in Figure 2(a). The observed signal, $S_{\beta\beta\alpha\alpha}^{\chi}$, has a linear relationship with the corresponding response function, but the factor depends on the configuration:

$$S_{\beta\beta\alpha\alpha}^{\chi} = A^{\chi} \times R_{\beta\beta\alpha\alpha}^{\chi}. \tag{2.37}$$

Thus S_{XXYY}^{χ} measured in a real experiment is likely to have a different absolute intensity scale from $S_{XXXX}^{\chi=0^\circ}$ and $S_{XXYY}^{\chi=0^\circ}$. The difference in the amplitudes of the signals must be accounted for. Equation (2.29) is useful for this purpose. What Eq. (2.29) means is that as long as all the polarizations are set so that they are X_L-polarized, the response functions should be the same in terms of the projection of the incident E-fields to transition dipole moment. Thus, when S_{XXXX}^{χ} is measured, the time dependence is identical to $S_{XXXX}^{\chi=0^\circ}$, but the amplitude is different due to the different sample configuration. By also measuring S_{XXXX}^{χ}, the necessary experimental amplitude correction factor can be obtained.

$$S_{XXXX}^{\chi} = (A^{\chi}/A^{\chi=0^\circ}) \times S_{XXXX}^{\chi=0^\circ}. \tag{2.38}$$

The measured S_{XXYY}^{χ} can be thus scaled using the $A^{\chi}/A^{\chi=0^\circ}$ as

$$S_{XXYY}^{\chi} \rightarrow (A^{\chi=0^\circ}/A^{\chi}) S_{XXYY}^{\chi}. \tag{2.39}$$

Then Eqs. (2.33)–(2.35) are used to obtain the orientational correlation functions and the population decay, by substituting $R_{\beta\beta\alpha\alpha}^{\chi}$ with measured $S_{\beta\beta\alpha\alpha}^{\chi}$ with the correct amplitudes. Therefore, although four measurements ($S_{XXXX}^{\chi=0^\circ}(t)$, $S_{XXYY}^{\chi=0^\circ}(t)$, $S_{XXYY}^{\chi}(t)$, and $\langle S \rangle$) are sufficient theoretically to extract all of the information, in practice a measurement of $S_{XXXX}^{\chi}(t)$ may also be necessary to scale $S_{XXYY}^{\chi}(t)$ to the correct amplitude. Then the scaled $S_{XXYY}^{\chi}(t)$ can be used with other two experimentally measured response functions.

Above, it has been shown that the experimental scheme to extract the orientational correlation function for three-dimensional isotropic samples (Eqs. (2.25) and (2.26)) is not applicable for two-dimensional monolayers. Instead of two measurements for isotropic samples, three time dependent measurements ($R_{XXXX}^{\chi=0^\circ}(t)$, $R_{XXYY}^{\chi=0^\circ}(t)$, and $R_{XXYY}^{\chi}(t)$) and one time averaged linear dichroism experiment to determine $\langle S \rangle$ are required for planar monolayers. In practice to correctly scale the amplitude of $R_{XXYY}^{\chi}(t)$, measurement of $R_{XXXX}^{\chi}(t)$

is also necessary. The results derived above show that the time-correlation functions for in-plane and out-of-plane motions can be independently obtained as $\langle Y_2^{2^*} Y_2^2 \rangle$ and $\langle Y_2^{0^*} Y_2^0 \rangle$ as seen in Eqs. (2.33)–(2.35).

III. MODEL CALCULATIONS OF THE ORIENTATIONAL RESPONSE FUNCTIONS FOR WOBBLING-IN-A-CONE

In this section model calculations are used to demonstrate how the structures and motions of molecules on a planar surface affect the response functions. In particular, we will focus on wobbling-in-a-cone motions of the transition dipoles.[6] Wobbling-in-a-cone model is known to capture the essential behavior of molecules under spatial restriction, which is the situation interfacial molecules are expected to experience. The transition dipoles can sample a range of angles that are within a cone of angles with cone half angle θ_C, which represents the extent of spatial restriction. There are two cases illustrated in Figures 3(a) and 3(b). The axis of the cone is normal to the plane (3(a)) and the axis of the cone has a tilt angle, θ_{tilt}, relative to the normal to the plane (3(b)).

If the axis of the cone is normal to the surface (normal cone), as shown in Figure 3(a), the polar angle θ of the transition dipole is restricted in the range $0 \leq \theta \leq \theta_C$, while no limitation is imposed on azimuthal angle ϕ. Wang and Pecora have given the averages and time-correlation functions of the spherical harmonics necessary to calculate the response functions and order parameters in Eqs. (2.21), (2.22), (2.28) and (2.31).[6] The averages and correlation functions of spherical harmonics are listed in Table II(A). In Sec. III A the orientational response functions for a transition dipole wobbling in a normal cone are presented for several θ_C.

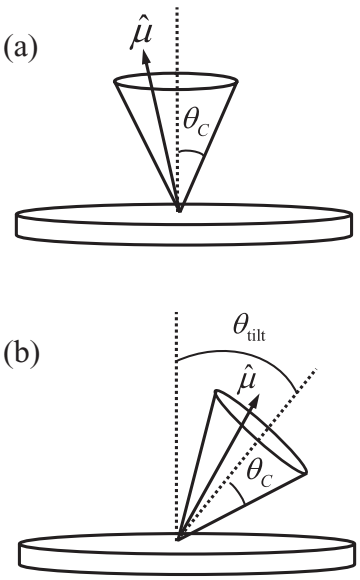

FIG. 3. Wobbling-in-a-cone model with cone half angle θ_C. (a) The cone axis is normal to the surface. (b) The cone axis is tilted by θ_{tilt} from Z_S axis (surface frame).

In general, the cone is likely to be tilted relative to the surface as shown in Figure 3(b). For a tilted cone, both the polar angle θ and the azimuthal angle ϕ are restricted. The averages and time correlation functions of the spherical harmonics associated with transition dipoles in tilted cones have been derived to calculate the response functions, and the results are shown in Table II(B). The derivations of the averages and correlation functions of the spherical harmonics are given in Section B of the supplementary material.[36] Based on the results given in Table II(B), the orientational response

TABLE II. Correlation functions and averages of spherical harmonics used to calculate the response functions in Eqs. (2.21), (2.22) and (2.32) for the wobbling-in-a-cone model. The order parameters, $\langle S \rangle$, can be calculated through Eq. (2.28) as well. D – diffusion constant, θ_C – (half) cone angle, and θ_{tilt} – tilt angle. ν_1, ν_2 are constants dependent on the cone angle θ_C. ν_1, ν_2 are well-approximated by $\nu_1 \approx 10^{0.496}\theta_C^{-1.122}$ and $\nu_2 \approx 10^{0.237}\theta_C^{-1.122}$. Refer to Section B in the supplementary material for the derivation of these correlation functions.[36]

A. Normal cone ($\theta_{tilt} = 0^\circ$)

$$\langle Y_2^{0^*}(t) Y_2^0(0) \rangle = \tfrac{5}{16\pi} \cos^2\theta_C (1+\cos\theta_C)^2 + \tfrac{1}{16\pi}(4 - \cos\theta_C - 6\cos^2\theta_C - \cos^3\theta_C + 4\cos^4\theta_C) e^{-\nu_1(\nu_1+1)Dt}$$

$$\langle Y_2^{2^*}(t) Y_2^2(0) \rangle = \tfrac{1}{32\pi}\{8 - 7\cos\theta_C(1+\cos\theta_C) + 3\cos^3\theta_C(1+\cos\theta_C)\} e^{-\nu_1(\nu_1+1)Dt}$$

$$\langle Y_2^0 \rangle = \sqrt{\tfrac{5}{16\pi}} \cos\theta_C (1+\cos\theta_C)$$

B. Tilted cone ($\theta_{tilt} \neq 0^\circ$)

$$\begin{aligned}\langle Y_2^{0^*}(t) Y_2^0(0) \rangle = {} & \tfrac{5}{320\pi}(3\cos^2\theta_{\text{tilt}} - 1)^2 [5\cos^2\theta_C (1+\cos\theta_C)^2. \\ & + (4 - \cos\theta_C - 6\cos^2\theta_C - \cos^3\theta_C + 4\cos^4\theta_C) e^{-\nu_1(\nu_1+1)Dt}] \\ & + \tfrac{3}{8\pi}\sin^2\theta_{\text{tilt}}\cos^2\theta_{\text{tilt}}\{2 + 2\cos\theta_C(1+\cos\theta_C) - 3\cos^3\theta_C(1+\cos\theta_C)\} e^{-\nu_2(\nu_2+1)Dt} \\ & + \tfrac{3}{128\pi}\sin^4\theta_{\text{tilt}}\{8 - 7\cos\theta_C(1+\cos\theta_C) + 3\cos^3\theta_C(1+\cos\theta_C)\} e^{-\nu_1(\nu_1+1)Dt}\end{aligned}$$

$$\begin{aligned}\langle Y_2^{2^*}(t) Y_2^2(0) \rangle = {} & \tfrac{3}{128\pi}\sin^4\theta_{\text{tilt}}[5\cos^2\theta_C(1+\cos\theta_C)^2 \\ & + (4 - \cos\theta_C - 6\cos^2\theta_C - \cos^3\theta_C + 4\cos^4\theta_C) e^{-\nu_1(\nu_1+1)Dt}] \\ & + \tfrac{1}{16\pi}\sin^2\theta_{\text{tilt}}(1+\cos^2\theta_{\text{tilt}}) \\ & \times \{2 + 2\cos\theta_C(1+\cos\theta_C) - 3\cos^3\theta_C(1+\cos\theta_C)\} e^{-\nu_2(\nu_2+1)Dt} \\ & + \tfrac{1}{32\pi}\{\sin^8\tfrac{\theta_{\text{tilt}}}{2} + \cos^8\tfrac{\theta_{\text{tilt}}}{2}\} \\ & \times \{8 - 7\cos\theta_C(1+\cos\theta_C) + 3\cos^3\theta_C(1+\cos\theta_C)\} e^{-\nu_1(\nu_1+1)Dt}\end{aligned}$$

$$\langle Y_2^0 \rangle = \sqrt{\tfrac{5}{16\pi}}\,\tfrac{3\cos^2\theta_{\text{tilt}} - 1}{2} \cos\theta_C (1+\cos\theta_C)$$

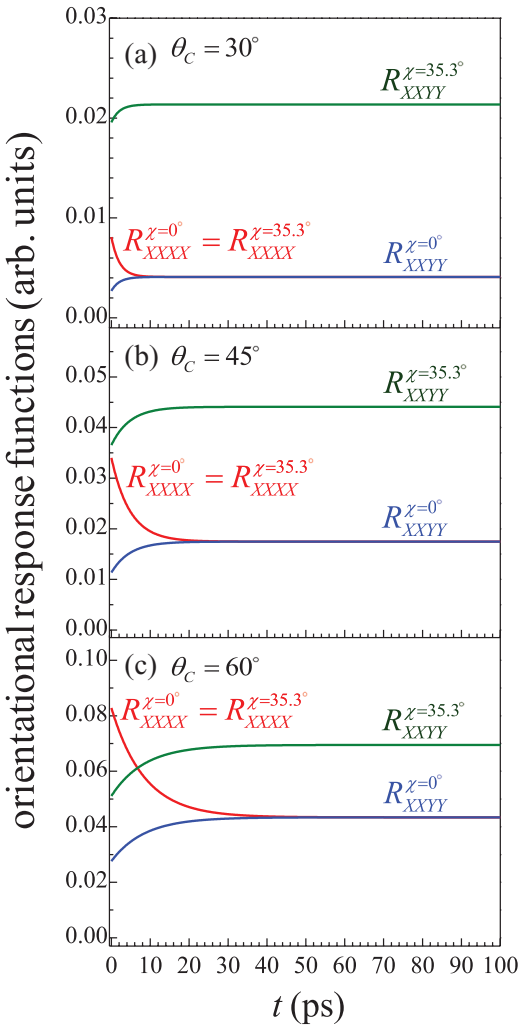

FIG. 4. Calculated orientational response functions for transition dipoles wobbling-in-a-normal-cone with various cone angles $\theta_C = 30°$, 45°, 60°. The diffusion constant D was set to 0.01 ps^{-1} for all cases. Red: $R_{XXXX}^{\chi=0°} = R_{XXXX}^{\chi=35.3°}$, blue: $R_{XXYY}^{\chi=0°}$, and green: $R_{XXYY}^{\chi=35.3°}$. Regardless of the cone angle θ_C, $R_{XXXX}^{\chi=0°}$ and $R_{XXYY}^{\chi=0°}$ reach the same level after long time. The depolarization rate decreases as the cone angle θ_C increases. The intensity level of $R_{XXYY}^{\chi=35.3°}$ is distinctively larger than $R_{XXXX}^{\chi=0°}$ and $R_{XXYY}^{\chi=0°}$ for small θ_C.

functions for a tilted cone are presented for several θ_{tilt}. In this section and Sec. IV, the surface to which molecules are bound is taken to be ideally flat. The effect of surface roughness will be discussed at the end of Sec. IV.

As is clear in Figure 3(b), for a tilted cone, the restriction imposed on the azimuthal angle ϕ is dependent on the polar angle θ. Thus in general, it is not valid to assume that polar and azimuthal motions of molecules are decoupled. The theory presented in Sec. II is applicable for general motions where polar and azimuthal motions are strongly correlated.

A. Transition dipole moments wobbling in a normal cone

The orientational response functions Eqs. (2.21), (2.22) and (2.32) calculated for a transition dipole wobbling in a normal cone (Figure 3(a)) with various cone angles are plotted in Figure 4. The diffusion constant D was set to 0.01 ps^{-1} for all cases. The response functions for parallel ($R_{XXXX}^{\chi=0°}$) and perpendicular ($R_{XXYY}^{\chi=0°}$) signals with the incident beam normal to the surface (Figure 2(a)) and the perpendicular signal ($R_{XXYY}^{\chi=35.3°}$) with the incident angle $\chi = 35.3°$ (Figure 2(b)) are shown in Figure 4. $R_{XXXX}^{\chi=35.3°}$ is the same as $R_{XXXX}^{\chi=0°}$ in small crossing angle limit. The order parameters, which can be measured with time averaged linear dichroism experiments, were also calculated and are tabulated in Table III(A), together with the average polar angles calculated from the order parameters.

TABLE III. Order parameters and corresponding average polar angles for a transition dipole wobbling in (A) a normal cone with various cone angles θ_C and (B) a tilted cone with various tilt angles θ_{tilt}. For calculation of tilted cone cases, the cone angle is fixed at $\theta_C = 30°$.

A. Normal cone ($\theta_{\text{tilt}} = 0°$)			
Cone angle θ_C	30°	45°	60°
Order parameter $\langle S \rangle$[a]	0.808	0.603	0.375
Average polar angle θ_{avg}[b]	21.0°	31.0°	40.2°
B. Tilted cone ($\theta_C = 30°$)			
Tilt angle θ_{tilt}	0°	30°	60°
Order parameter $\langle S \rangle$[a]	0.808	0.505	−0.101
Average polar angle θ_{avg}[b]	21.0°	35.1°	59.0°

[a]Calulated by $\langle S \rangle = \sqrt{4\pi/5}\langle Y_2^0 \rangle$. See Section B of the supplementary material.[36]
[b]Calculated by solving $\langle S \rangle = (3\cos^2\theta_{\text{avg}} - 1)/2$.

A prominent feature observed in Figure 4 is that $R_{XXXX}^{\chi=0°}$ and $R_{XXYY}^{\chi=0°}$ tend to be smaller than $R_{XXYY}^{\chi=35.3°}$. For normal cones with small θ_C, the transition dipoles on the surface tend to be normal to the surface, and in case incident polarizations are in-plane, the transition dipole moments cannot interact sufficiently with the E-fields. As θ_C increases, the average polar angle also becomes larger (Table III(A)). As a result the difference between $R_{XXYY}^{\chi=35.3°}$ and the other two, $R_{XXXX}^{\chi=0°}$ and $R_{XXYY}^{\chi=0°}$, becomes smaller. It can also be seen in Figure 4 that regardless of the cone angle θ_C, $R_{XXXX}^{\chi=0°}$ and $R_{XXYY}^{\chi=0°}$ reach the same intensity level after long time. The physical meaning of this behavior is important and can be traced back to Eqs. (2.21) and (2.22). Subtracting Eq. (2.22) from Eq. (2.21), $R_{XXXX}^{\chi=0°} - R_{XXYY}^{\chi=0°} \propto \langle Y_2^{2^*} Y_2^2 \rangle$ is obtained. As discussed in Sec. II, $\langle Y_2^{2^*} Y_2^2 \rangle$ is essentially the orientational correlation function for in-plane motion. Thus, in the absence of population decay, $R_{XXXX}^{\chi=0°} - R_{XXYY}^{\chi=0°}$ is recording the in-plane orientational correlation function. For a transition dipole wobbling in a cone with its axis normal to the plane, the azimuthal angle ϕ will completely randomize after sufficiently long time because there is no restriction on in-plane motion. Therefore, the in-plane orientational correlation function, $\langle Y_2^{2^*} Y_2^2 \rangle$, will decay to zero ($R_{XXXX}^{\chi=0°} = R_{XXYY}^{\chi=0°}$ at long time) independent of the cone angle θ_C. If the anisotropy $r(t)$ given in Eq. (1.1) is calculated from the measurements of $R_{XXXX}^{\chi=0°}$ and $R_{XXYY}^{\chi=0°}$ in the conventional single geometry shown in Figure 2(a), $r(t)$ will decay to zero regardless of the cone angle. Therefore, anisotropy $r(t)$ contains no information on the cone angle θ_C. To extract the cone angle, the measurements with the two geometries shown in Figures 2(a) and 2(b) are necessary, and the two orientational correlation functions must be obtained using Eqs. (2.34) and (2.35). The detailed procedure to derive the cone angle will be discussed in Sec. IV.

Another important feature of the response functions shown in Figure 4 is the dependence of the depolarization

time constants on the cone angle θ_C. As seen in Figure 4, transition dipoles wobbling in a cone with smaller θ_C tend to complete depolarization faster than transition dipoles with larger θ_C, even with the same diffusion constant, $D = 0.01$ ps^{-1}. For example, for $\theta_C = 30^\circ$ cone, $R^{\chi=0^\circ}_{XXXX} - R^{\chi=0^\circ}_{XXYY}$ reaches zero within ~10 ps, whereas it takes nearly ~50 ps for $\theta_C = 60^\circ$. Therefore, the determination of the diffusion constant requires the information on both the depolarization time constant and the θ_C. This is also true for wobbling-in-a-cone in an isotropic 3D system.[5] It is also important that all the response functions are single exponential decays, because the time dependence of correlation functions in Table II(A) are described only by $\exp[-\nu_1(\nu_1+1)Dt]$.

B. Transition dipole moments wobbling in a tilted cone

Orientational response functions from Eqs. (2.21), (2.22) and (2.32) are calculated for a transition dipole wobbling in a tilted cone (Figure 3(b)). The correlation functions and average of spherical harmonics in Table II(B) were employed for the calculations. θ_C was fixed at 30° and the tilt angle θ_{tilt} was varied from 0° (no tilt) to 60°. Time-independent order parameters and average polar angle are listed in Table III(B).

The relative intensity of $R^{\chi=35.3^\circ}_{XXYY}$ with respect to $R^{\chi=0^\circ}_{XXXX}$ and $R^{\chi=0^\circ}_{XXYY}$ can be explained in a similar way as in the normal cone case. As tilt angle θ_{tilt} increases, the average polar angle of transition dipole moments on the surface also increases. As a result, $R^{\chi=0^\circ}_{XXXX}$ and $R^{\chi=0^\circ}_{XXYY}$ tend to increase due to larger projection of incident E-field onto the transition dipoles, while $R^{\chi=35.3^\circ}_{XXYY}$ decreases relative to $R^{\chi=0^\circ}_{XXXX}$ and $R^{\chi=0^\circ}_{XXYY}$ as average polar angle increases.

The most important feature in Figure 5 is that for $\theta_{\text{tilt}} > 0^\circ$, $R^{\chi=0^\circ}_{XXXX}$ and $R^{\chi=0^\circ}_{XXYY}$ (geometry of Figure 2(a)) are not equal even after infinitely long time. Again, $R^{\chi=0^\circ}_{XXXX} - R^{\chi=0^\circ}_{XXYY} \propto \langle Y_2^{2^*} Y_2^2 \rangle$ is reporting on the in-plane orientational correlation function. In the case of normal cone discussed above, $\langle Y_2^{2^*} Y_2^2 \rangle$ decays to zero. However, for a tilted cone, both the out-of-plane and in-plane motions are limited. It is clear from Figure 3(b) that a transition dipole cannot sample all the azimuthal angles in the surface frame, leading to a plateau in $\langle Y_2^{2^*} Y_2^2 \rangle$ at long time. Thus $R^{\chi=0^\circ}_{XXXX} - R^{\chi=0^\circ}_{XXYY}$ is non-zero even at long time. Larger θ_{tilt} produces more restriction on the azimuthal motion of the transition dipole, and the difference between $R^{\chi=0^\circ}_{XXXX}$ and $R^{\chi=0^\circ}_{XXYY}$ becomes more significant. The restriction on azimuthal angles also depends on cone angle θ_C. Again, three measurements, $R^{\chi=0^\circ}_{XXXX}$, $R^{\chi=0^\circ}_{XXYY}$ and $R^{\chi=35.3^\circ}_{XXYY}$, are required to independently obtain θ_{tilt} and θ_C. The details of the determination will be discussed in Sec. IV.

It should be clear from the above discussions that if the anisotropy $r(t)$ (Eq. (1.1)) is measured in the configuration shown in Figure 2(a), a non-zero plateau in $r(t)$ indicates that wobbling is occurring in a tilted cone rather than a normal cone, even though further quantitative information cannot be obtained from $r(t)$.

The time dependence of the response functions shows complicated behavior in the case of a tilted cone. As seen in Table II(B), the spherical harmonics correlation functions used in the calculations of the response functions are bi-exponential (with $\exp[-\nu_1(\nu_1+1)Dt]$ and $\exp[-\nu_2(\nu_2+1)Dt]$). Therefore, the response functions constructed from these correlation functions are also bi-exponential. Even though ν_1 and ν_2 only depend on θ_C, the ratio of the amplitudes of the two exponentials depends both on θ_{tilt} and θ_C. The details of the time dependence are discussed immediately below.

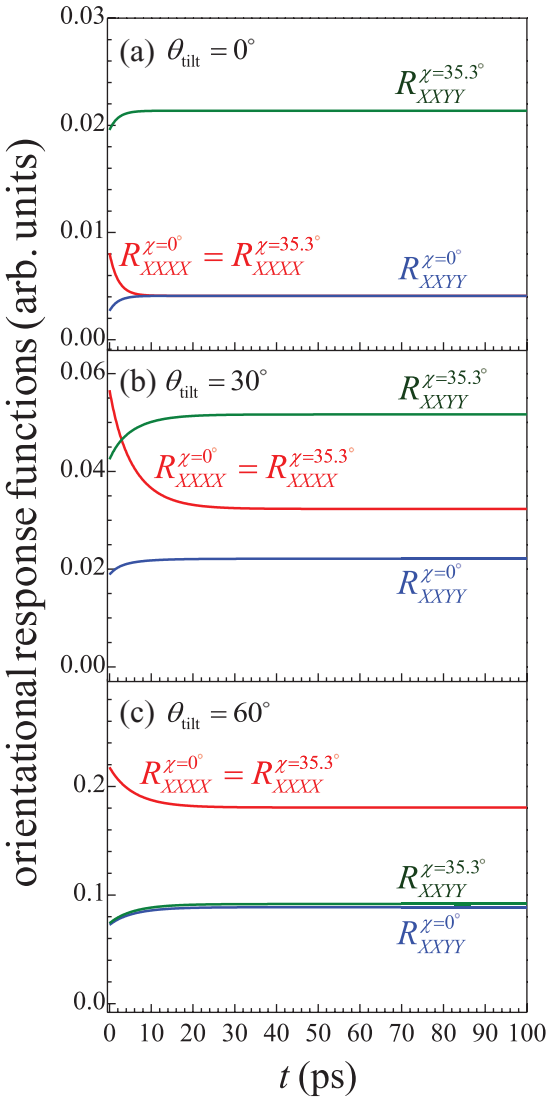

FIG. 5. Calculated orientational response functions for transition dipoles for tilted cone wobbling with tilt angles $\theta_{\text{tilt}} = 0^\circ$(no tilt), 30°, 60°. The cone angle θ_C and the diffusion constant D were set to 30° and 0.01 ps^{-1}, respectively. Red: $R^{\chi=0^\circ}_{XXXX} = R^{\chi=35.3^\circ}_{XXXX}$, blue: $R^{\chi=0^\circ}_{XXYY}$, and green: $R^{\chi=35.3^\circ}_{XXYY}$. In contrast to cones with their axes normal to the plane, $R^{\chi=0^\circ}_{XXXX}$ and $R^{\chi=0^\circ}_{XXYY}$ are distinctively different even at infinite time.

IV. DEMONSTRATION OF DATA ANALYSIS PROCEDURE

A. Two model cases and recovery of the orientational correlation functions

In Sec. III, using Eqs. (2.21), (2.22) and (2.31), orientational response functions were calculated for transition

dipoles wobbling in various types of cones. The correlation functions of spherical harmonics given in Table II were employed. To obtain information from experiments, the reverse procedure needs to be employed. The response functions, $R^{\chi=0^\circ}_{XXXX}$, $R^{\chi=0^\circ}_{XXYY}$, and R^{χ}_{XXYY}, are measured as observables, and the correlation functions for spherical harmonics, $\langle Y_2^{0^*} Y_2^0 \rangle$ and $\langle Y_2^{2^*} Y_2^2 \rangle$, are reconstructed from these response functions by applying Eqs. (2.33)–(2.35). Based on the $\langle Y_2^{0^*} Y_2^0 \rangle$ and $\langle Y_2^{2^*} Y_2^2 \rangle$ obtained from the experiments, in the context of the wobbling-in-a-cone model, the cone angle θ_C and tilt angle θ_{tilt} can be extracted. In this section, the procedure is demonstrated by examining the following two model systems: a system in which transition dipoles are wobbling in a normal cone ($\theta_{\text{tilt}} = 0^\circ$) with $\theta_C = 60^\circ$, and another system where transition dipoles are wobbling in a tilted cone with $\theta_{\text{tilt}} = 36.7^\circ$ and $\theta_C = 30^\circ$. We refer to these two samples as systems A and B, respectively. The parameters for these two cases were selected because these two systems have the same order parameter $\langle S \rangle = 0.375$. Therefore, these two cases are not distinguishable based only on time averaged measurements, such as linear dichroism experiments, regardless of the significant differences in the structure and dynamics of the two systems. As shown in the following discussion, these two cases are clearly resolved by dynamic depolarization measurements described in Sec. II.

In Sec. III, only orientational response functions were included in the calculations. In real measurements there is also isotropic population decay ($P(t)$ in Eqs. (2.21), (2.22) and (2.31)). Here we assume that we are studying a vibrational probe with vibrational lifetime of 20 ps ($P(t) \propto \exp[-t/(20\text{ps})]$).

For both of the systems, $\langle Y_2^{0^*} Y_2^0 \rangle$ and $\langle Y_2^{2^*} Y_2^2 \rangle$ can be calculated using Table II. Here we set the orientational diffusion constant D to 0.01 ps^{-1} for both systems. Then, together with the isotropic population decay $P(t)$ with $\tau_V = 20$ ps, the total response functions can be calculated based on Eqs. (2.21), (2.22) and (2.31). The actual functional form of $P(t)$, $\langle Y_2^{0^*} Y_2^0 \rangle$, and $\langle Y_2^{2^*} Y_2^2 \rangle$ used to calculate the response functions are given in Table IV, and the resultant response functions are plotted in Figure 6(a) for system A and Figure 6(b) for system B.

The goal of the dynamic depolarization experiments is to obtain τ_V, θ_C, θ_{tilt}, and D for the systems based on the "signals" in Figure 6. To find these parameters, $P(t)$, $\langle Y_2^{0^*} Y_2^0 \rangle$, and $\langle Y_2^{2^*} Y_2^2 \rangle$ must be extracted using Eqs. (2.33)–(2.35). $P(t)$, $\langle Y_2^{0^*} Y_2^0 \rangle$, and $\langle Y_2^{2^*} Y_2^2 \rangle$ obtained using Eqs. (2.33)–(2.35) are shown in Figure 7.

As seen in Figure 6, the difference between the response functions for these two systems is significant but not large, especially due to the presence of population decay $P(t)$. However, once $P(t)$, $\langle Y_2^{0^*} Y_2^0 \rangle$, and $\langle Y_2^{2^*} Y_2^2 \rangle$ are independently recovered from the response functions, these two systems display very different behavior of $\langle Y_2^{2^*} Y_2^2 \rangle$ as shown in Figure 7. Thus, in many instances, extracting the orientational correlation functions is more useful than directly comparing the response functions.

The population decays (calculated using Eq. (2.33) from the plots in Figure 6) shown in Figure 7(a) (blue and red dashed curves) correctly recovers the single exponential population decay with the vibrational lifetime of $\tau_V = 20$ps. In these model calculations it was assumed that the population decay is a single exponential, but the procedure shown here to extract population decay is valid regardless of the actual form of population decay as long as the population relaxation is independent of molecular orientation.

TABLE IV. Parameters used to calculate the response functions in Figure 6. Correlation functions listed in Table II were used to obtain these parameters. Based on these parameters, population decays and orientational correlation functions are constructed as $P(t) \propto \exp[-t/\tau_V]$, $\langle Y_2^{0^*}(t) Y_2^0(0) \rangle = A_{2,0}^{\text{fast}} \cdot e^{-t/\tau_{wf}} + A_{2,0}^{\text{slow}} \cdot e^{-t/\tau_{ws}} + A_{2,0}^{\infty}$, $\langle Y_2^{2^*}(t) Y_2^2(0) \rangle = A_{2,2}^{\text{fast}} \cdot e^{-t/\tau_{wf}} + A_{2,2}^{\text{slow}} \cdot e^{-t/\tau_{ws}} + A_{2,2}^{\infty}$. Note that for normal cone (system A) both of the orientational correlation functions decay with single exponentials, while the correlation functions for the tilted cone (system B) are bi-exponential decays. These parameters are correctly recovered from $P(t)$, $\langle Y_2^{0^*} Y_2^0 \rangle$ and $\langle Y_2^{2^*} Y_2^2 \rangle$ in Figure 7.

	System A	System B
τ_V (ps)	20	
τ_{wf} (ps)	8.3	2.1
τ_{ws} (ps)	...	6.3
$A_{2,0}^{fast}$	0.042	0.001
$A_{2,0}^{slow}$	...	0.044
$A_{2,0}^{\infty}$	0.056	0.056
$A_{2,2}^{fast}$	0.033	0.002
$A_{2,2}^{slow}$	...	0.019
$A_{2,2}^{\infty}$	0	0.012

Orientational correlation functions of our primary interest, $\langle Y_2^{0^*} Y_2^0 \rangle$ and $\langle Y_2^{2^*} Y_2^2 \rangle$, are shown in Figures 7(b) and 7(c),

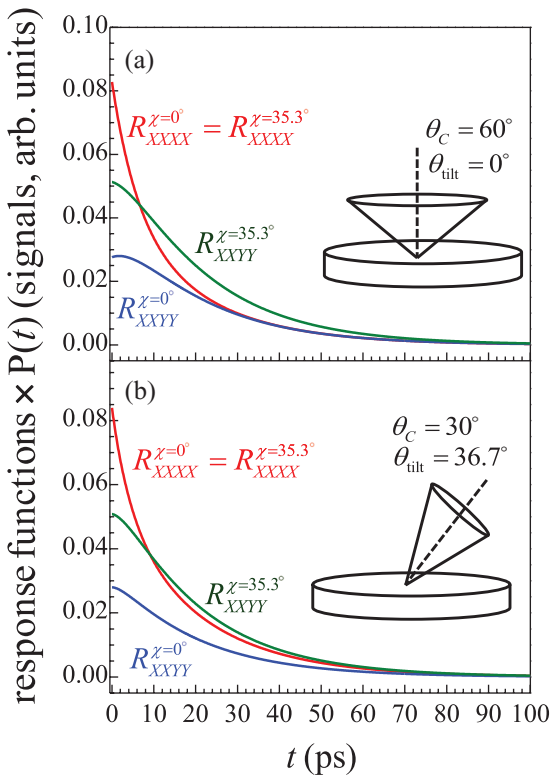

FIG. 6. Calculated response functions (signals) for (a) ($\theta_C = 60^\circ$, $\theta_{\text{tilt}} = 0^\circ$) and (b) ($\theta_C = 30^\circ$, $\theta_{\text{tilt}} = 36.7^\circ$) including the population decay $P(t)$ ($\tau_V = 20$ ps). Red: $R^{\chi=0^\circ}_{XXXX} = R^{\chi=35.3^\circ}_{XXXX}$, blue: $R^{\chi=0^\circ}_{XXYY}$, and green: $R^{\chi=35.3^\circ}_{XXYY}$.

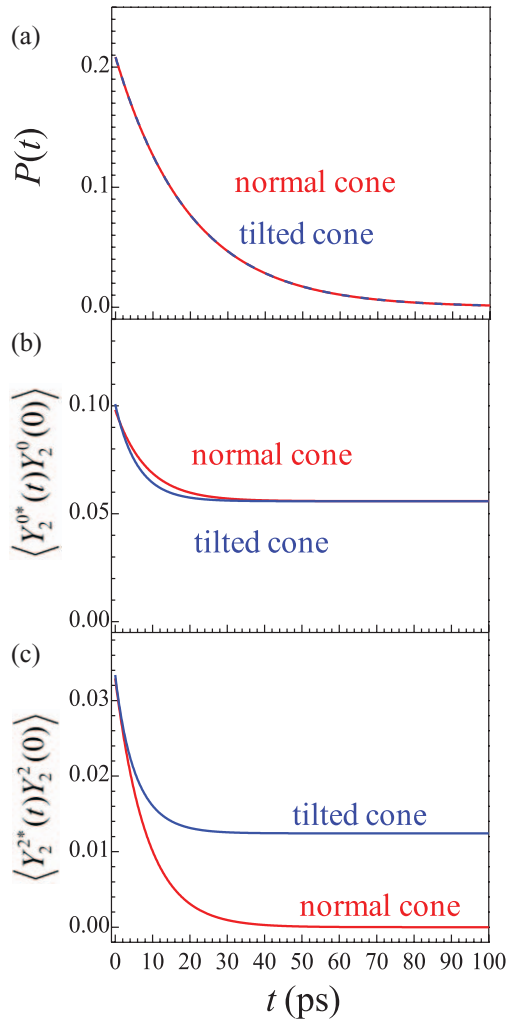

FIG. 7. Population decays $P(t)$ and the two orientational correlation functions, $\langle Y_2^{0^*} Y_2^0 \rangle$ and $\langle Y_2^{2^*} Y_2^2 \rangle$, recovered from the calculated data in Figure 6 using Eqs. (2.33)–(2.35). (a) Population decays (red dashed curve, normal cone; blue dashed curve, tilted cone) obtained with Eq. (2.33). (b) $\langle Y_2^{0^*} Y_2^0 \rangle$ for both systems obtained with Eq. (2.35). Similar and substantial plateau levels are observed for both systems. (c) $\langle Y_2^{2^*} Y_2^2 \rangle$ orientational correlation function obtained with Eq. (2.34). While $\langle Y_2^{2^*} Y_2^2 \rangle$ decays to zero for the normal cone, $\langle Y_2^{2^*} Y_2^2 \rangle$ reaches an offset significantly above zero for the tilted cone.

respectively. The difference between normal cone and tilted cone emerges particularly in $\langle Y_2^{2^*} Y_2^2 \rangle$, which can be interpreted as in-plane orientational correlation function. While $\langle Y_2^{2^*} Y_2^2 \rangle$ decays to zero for system A (normal cone), there is a significant plateau observed for system B (tilted cone). As mentioned in Sec. III, the physical origin of this behavior is clear. While there is no restriction on azimuthal angle ϕ in surface frame for normal cone (decays to zero), the directions of transition dipoles are azimuthally confined for a tilted cone (decays to a plateau). If $\langle Y_2^{2^*} Y_2^2 \rangle$ has a plateau, the cone is titled. $\langle Y_2^{0^*} Y_2^0 \rangle$ is also different for the normal and tilted cones, but the difference is not large for the particular parameters used in these calculations.

B. Extraction of cone angle and tilt angle

θ_C and θ_{tilt} can be determined from data like those shown in Figure 7. For an isotropic three-dimensional system, the cone angle θ_C can be extracted from the offset in the anisotropy $r(t)$. For planar monolayers, offsets in both $\langle Y_2^{2^*} Y_2^2 \rangle$ and $\langle Y_2^{0^*} Y_2^0 \rangle$ are necessary to obtain θ_C and θ_{tilt}. As shown in Section B of the supplementary material,[36] the correlation functions at infinitely long time (the plateaus) are given by

$$\left\langle Y_2^{2^*}(\infty) Y_2^2(0) \right\rangle = \frac{15}{128\pi} \sin^4 \theta_{\text{tilt}} \cos^2 \theta_C \, (1 + \cos \theta_C)^2 \,, \tag{4.1}$$

$$\left\langle Y_2^{0^*}(\infty) Y_2^0(0) \right\rangle = \frac{5}{64\pi} (3 \cos^2 \theta_{\text{tilt}} - 1)^2 \cos^2 \theta_C (1 + \cos \theta_C)^2 . \tag{4.2}$$

Dividing Eq. (4.1) by Eq. (4.2),

$$\frac{\left\langle Y_2^{2^*}(\infty) Y_2^2(0) \right\rangle}{\left\langle Y_2^{0^*}(\infty) Y_2^0(0) \right\rangle} = \frac{3}{2} \cdot \left(\frac{\sin^2 \theta_{\text{tilt}}}{3 \cos^2 \theta_{\text{tilt}} - 1} \right)^2 . \tag{4.3}$$

Therefore, θ_{tilt} can be extracted from the offsets in the two spherical harmonics correlation functions. The plateau level for $\langle Y_2^{2^*} Y_2^2 \rangle$ is zero for system A, so $\theta_{\text{tilt}} = 0°$. For system B, $\langle Y_2^{2^*}(\infty) Y_2^2(0) \rangle / \langle Y_2^{0^*}(\infty) Y_2^0(0) \rangle = 0.21$, so $\theta_{\text{tilt}} = 36.7°$, which is consistent with the input in the model calculations.

Once the tilt angle θ_{tilt} is derived, putting it into Eq. (4.1) or (4.2), θ_C is extracted. For sample A, because $\langle Y_2^{0^*}(\infty) Y_2^0(0) \rangle = 0.056$ and $\theta_{\text{tilt}} = 0°$, $\cos^2 \theta_C (1 + \cos \theta_C)^2 = 0.56$ from Eq. (4.2), giving $\theta_C = 60°$. Similarly, the cone angle for system B is calculated from Eq. (4.1) to be 30°.

While the procedure mentioned above works in a straightforward manner for these two systems, careful attention must be paid in case the derived offset ratio $\langle Y_2^{2^*}(\infty) Y_2^2(0) \rangle / \langle Y_2^{0^*}(\infty) Y_2^0(0) \rangle$ exceeds 1.5, because there are two possible values of θ_{tilt} which yield the same offset ratio given in Eq. (4.3). One of the solutions of Eq. (4.3) is smaller than 54.7°, while another solution is larger than 54.7°. To determine θ_{tilt} uniquely, the sign of order parameter $\langle S \rangle$ can be employed. For transition dipole moments wobbling-in-a-cone, $\langle S \rangle$ is given by

$$\langle S \rangle = \frac{3 \cos^2 \theta_{\text{tilt}} - 1}{2} \cos \theta_C (1 + \cos \theta_C) . \tag{4.4}$$

Assuming $\theta_C < 90°$, the sign of $\langle S \rangle$ is determined only by $(3 \cos^2 \theta_{\text{tilt}} - 1)/2$. Therefore by obtaining the sign of order parameter $\langle S \rangle$ through linear dichroism measurement, θ_{tilt} can be determined to be either larger or smaller than 54.7°. Then together with the value of $\langle Y_2^{2^*}(\infty) Y_2^2(0) \rangle / \langle Y_2^{0^*}(\infty) Y_2^0(0) \rangle$, θ_{tilt} can be uniquely specified.

The offset ratio given in Eq. (4.3) is quite sensitive to θ_{tilt} when θ_{tilt} is larger than 30°, which enables a precise determination of θ_{tilt}. If θ_{tilt} is smaller than 20° the offset ratio is close to zero and is less sensitive to θ_{tilt}, which will lead to less accuracy in the determination of θ_{tilt}.

C. Extraction of diffusion constant *D*

Another important parameter contained in the spherical harmonics correlation functions is the orientational diffusion constant D. For a three dimensional system in which the molecular orientation is completely randomized, the constant

can be extracted by $D = 1/6\tau$, where τ is the time constant for decay of the anisotropy. For a three-dimensional isotropic wobbling-in-a-cone system, the diffusion constant can be extracted from the single exponential anisotropy decay time constant τ_w by[5]

$$D \approx \frac{7\theta_C^2}{24\tau_w}, \tag{4.5}$$

where θ_C is the cone angle obtained from the plateau level in the anisotropy. Thus for wobbling-in-a-cone model, the diffusion constant depends both on τ_w and θ_C.

The situation is more complicated for molecules functionalized on a planar surface. For transition dipoles wobbling-in-a-cone, Table II shows that $\langle Y_2^{0^*} Y_2^0 \rangle$ and $\langle Y_2^{2^*} Y_2^2 \rangle$ decay as bi-exponentials,

$$\left\langle Y_2^{0^*}(t) Y_2^0(0) \right\rangle = A_{20}^{\text{fast}} \cdot e^{-t/\tau_{wf}} + A_{20}^{\text{slow}} \cdot e^{-t/\tau_{ws}} + A_{20}^{\infty}, \tag{4.6}$$

$$\left\langle Y_2^{2^*}(t) Y_2^2(0) \right\rangle = A_{22}^{\text{fast}} \cdot e^{-t/\tau_{wf}} + A_{22}^{\text{slow}} \cdot e^{-t/\tau_{ws}} + A_{22}^{\infty}, \tag{4.7}$$

where τ_{wf} and τ_{ws} are the faster and slower wobbling time constants. The decay time constants are related to the cone angle by

$$\tau_{wf} \approx \frac{1}{\nu_1(\theta_C)\,(\nu_1(\theta_C)+1)\,D}, \tag{4.8}$$

$$\tau_{ws} \approx \frac{1}{\nu_2(\theta_C)\,(\nu_2(\theta_C)+1)\,D}, \tag{4.9}$$

with

$$\nu_1(\theta_C) = 10^{0.496}\theta_C^{-1.122}, \tag{4.10}$$

$$\nu_2(\theta_C) = 10^{0.237}\theta_C^{-1.122}. \tag{4.11}$$

As seen in Eqs. (4.10) and (4.11), ν_1 is roughly ~1.8 times larger than ν_2. Note that the ratio of the amplitudes of the fast decay component and the slow decay component depends both on θ_C and θ_{tilt}, as given in Table II(B). The ratios of the amplitudes, $A_{20}^{\text{slow}}/A_{20}^{\text{fast}}$ and $A_{22}^{\text{slow}}/A_{22}^{\text{fast}}$, are shown in Figure 8 for various tile angles θ_{tilt} with the cone angle fixed to $\theta_C = 30^\circ$ or 60°.

For system A, θ_C and θ_{tilt} are 60° and 0°, respectively. As seen in Figure 8, if $\theta_C = 60^\circ$ and θ_{tilt} is small, the contribution from slow component is negligible and the decay in both $\langle Y_2^{0^*} Y_2^0 \rangle$ and $\langle Y_2^{2^*} Y_2^2 \rangle$ can be regarded as single exponential decays with the fast decay time. (For the normal cone, the decay is rigorously single exponential as can be seen in Table II(A)). Equation (4.10) yields $\nu_1(60^\circ) = 2.98$. Then based on the decay time constant of $\tau_{wf} = 8.3$ ps for both $\langle Y_2^{0^*} Y_2^0 \rangle$ and $\langle Y_2^{2^*} Y_2^2 \rangle$ (Table IV), the diffusion constant D can be correctly recovered as 0.01 ps^{-1}, using Eq. (4.8).

For system B with $\theta_C = 30^\circ$ and $\theta_{\text{tilt}} = 36.7^\circ$, which can be experimentally derived from the ratio of plateaus in orientational correlation functions, the contribution from the fast component is negligible for both $\langle Y_2^{0^*} Y_2^0 \rangle$ and $\langle Y_2^{2^*} Y_2^2 \rangle$ as seen in Figures 8(a) and 8(b), and the decay will appear to be single exponential with the decay time constant of 6.3 ps (Table IV). Knowing that this time constant corresponds to slow decay time constant τ_{ws}, the diffusion time constant D can be correctly recovered as 0.01 ps^{-1}, using Eq. (4.9) and $\nu_2(30^\circ) = 3.57$.

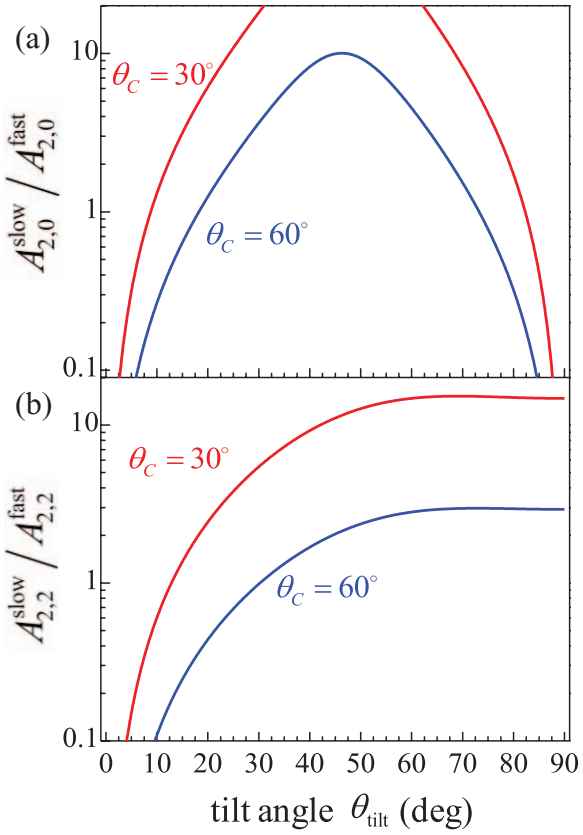

FIG. 8. The amplitude ratio (a) $A_{20}^{\text{slow}}/A_{20}^{\text{fast}}$ and (b) $A_{22}^{\text{slow}}/A_{22}^{\text{fast}}$ in Eqs. (4.6) and (4.7) with respect to the tilt angle θ_{tilt} for two cone angles $\theta_C = 30^\circ$ (red) and 60° (blue). Table II(B) can be used to calculate the ratios for other sets of cone and tilt angles.

D. Surface roughness

When a monolayer on a solid substrate is studied, the surface supporting the monolayer may not be ideally flat, and has some roughness. As mentioned in Sec. II, the procedure presented there (and in Sec. V) to extract in-plane and out-of-plane orientational correlation functions is totally valid even for the molecules on rough surfaces, as long as the roughness is symmetric in plane and thus the system can be regarded as a uniaxial system. If not specifically taken into account, the roughness will become part of the angular distribution and the effect is convolved into the obtained orientational correlation functions. Surface roughness essentially tilts the transition dipole moments by some range of angles about those that would occur in the ideally flat case. If the roughness amounts to a range of a few degrees, it could be ignored and the results in Secs. III and IV can be directly employed. In case the surface is locally and significantly rough, the roughness should be taken into account to simulate or interpret $\langle Y_2^{2^*} Y_2^2 \rangle$ and $\langle Y_2^{0^*} Y_2^0 \rangle$. Once the nature of the surface roughness is

characterized, e.g., using Atomic Force Microscopy, it is straightforward to simulate $\langle Y_2^{2^*} Y_2^2 \rangle$ and $\langle Y_2^{0^*} Y_2^0 \rangle$ with the surface roughness taken into account. This procedure is briefly discussed in Section B of the supplementary material.[36] Roughness is obviously not the issue for studying dynamics at liquid-air interfaces, or uniaxial thick samples such as liquid crystals.

Thus the surface roughness can be rigorously accounted for, but it is worth showing that the effect of surface roughness is minor if monolayer samples are prepared with reasonably high quality substrates. Commercially available substrates have the surface flatness of $\lambda/10$, meaning that peak-to-valley depth on surface is ~50 nm. What is important here is the horizontal length scale (in the plane) over which this peak-to-valley roughness is occurring. In case this peak-to-valley roughness happens over 10 μm, the actual surface to which molecules are bound is tilted by at most $\sim 0.2^\circ$. This angle is so small that the surface can be regarded as ideally flat, and the discussion in Secs. III and IV will be directly applicable. If the peak-to-valley roughness has a period of 1 μm, the surface can be tilted by $\sim 3^\circ$, which may still be regarded as relatively small angle, but the roughness can be taken into account rigorously by applying the formula given in the supplementary material.[36] Monolayers on rougher surfaces should definitely be treated with the consideration of surface roughness. As seen in the discussion above, what matters is the absolute roughness of the substrate's surface (range of angles about the ideal plane), and the thickness of the monolayer relative to the peak-to-valley depth is not important.

V. NON-COLLINEAR BEAM GEOMETRIES

To this point the theoretical developments have been for experimental configurations in the small crossing angle limit. In the small crossing angle limit, the response functions are given by Eqs. (2.21), (2.22) and (2.31). The correlation functions of the spherical harmonics and isotropic population decay are obtained by solving these equations through Eqs. (2.33)–(2.35). In the real experiments, however, non-negligible crossing angles are frequently required to separate the signal from pump beam(s) or, in a fluorescence experiment, to observe a cone of emitted fluorescence.

In the case that the crossing angle between the beams is significant, the polarizations of the beams (X or Y) do not necessarily coincide with the polarizations in lab frame defined in Figure 2, and the corrections to the formulas are required that depend on the crossing angle. In this section, we will present the formulas for the orientational response functions for the following four beam geometries: pump-probe geometry, transient grating geometry with the beams in a plane, BOXCARS geometry, and fluorescence geometry. The derivations of these formulas are provided in detail in Section C of the supplementary material.[36] In the following, the monolayer sample is on the front surface of the substrate, and thus the beams in Figures 9 and 10 do not show the refraction that will occur when the beams pass in and out of the substrate.

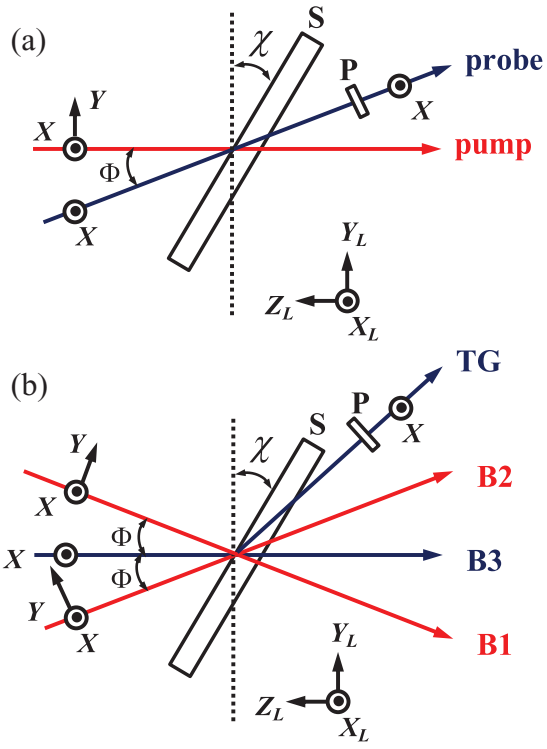

FIG. 9. Experimental geometries for (a) pump-probe geometry and (b) heterodyne detected transient grating geometry with beams in a single plane. S-sample with the monolayer on the input side of the substrate, P- polarizer to set the signal's polarization. In both (a) and (b), the sample is tilted in $Y_L Z_L$ plane. For the pump-probe geometry (a), the polarization of each beam exactly coincides with the polarization in lab frame. For the HDTG geometry (b), while the X-polarization of each beam coincides with the X_L-polarization in lab frame, the Y-polarization is a linear combination of the Y_L- and Z_L-polarizations.

A. Pump-probe geometry

In the pump-probe geometry, the only crossing angle is the angle between the pump and probe beams. There are several possible ways to set the polarizations and install the planar sample, but the simplest configuration is shown in Figure 9(a). In Figure 9(a), the k-vectors for the pump and probe beams are in $Y_L Z_L$ plane. The k-vector for pump beam is set so that it is normal to the surface when $\chi = 0^\circ$. Also, the polarization of probe beam is fixed so that it is parallel to X_L axis. Note that, as shown in Figure 9(a), the polarizations of the beams (X or Y) exactly coincide with the polarizations in lab frame (X_L and Y_L), regardless of the crossing angle Φ. So whatever Φ is, the discussion shown in Sec. II C is applicable without any modifications; the response functions are given by Eqs. (2.21), (2.22) and (2.31), and the orientational correlation functions can be calculated by Eqs. (2.33)–(2.35).

B. Heterodyne detected transient grating geometry with beams in a plane

In heterodyne detected transient grating experiment, the same information as pump-probe experiment can be acquired with the improved sensitivity.[33,44] The geometry with the three excitation beams and the signal beam in a plane is shown

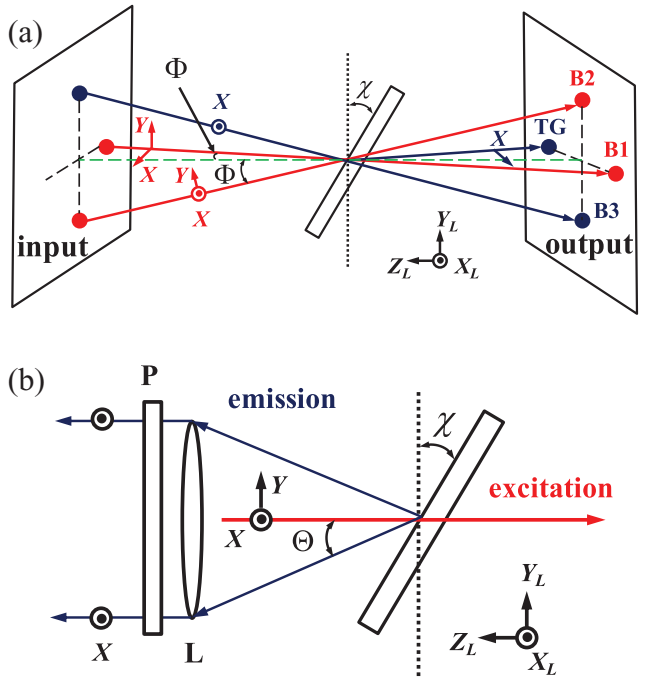

FIG. 10. The beam geometry for (a) heterodyne detected transient grating in the BOXCARS geometry and (b) fluorescence experimental geometry. In (a), beam 1 and the TG signal beam are in the X_LZ_L plane; beams 2 and 3 are crossed in Y_LZ_L plane. The sample is installed so that Z_S axis in the surface frame is normal to the X_L axis. The Z_S axis in the surface frame is tilted by angle χ with respect to the Z_L axis. The angles Φ are relative to the dashed green line in (a), which is perpendicular to the input plane and is equidistant from each of the input beams, B1, B2, and B3. In (b) both X and Y polarizations of the excitation beam are along the X_L and Y_L axes in lab frame, respectively. The sample is installed so that Z_S axis in the surface frame is normal to X_L axis. The sample is tilted so that the Z_S axis makes an angle χ with Z_L axis. The cone of emitted fluorescence is collected by the lens (L), and then passed through the polarizer (P). The half-cone angle of the collected fluorescence is Θ.

in Figure 9(b). The two excitation pulses (beams B1 and B2) cross in the sample simultaneously to produce the grating. The third beam (B3) is the probe beam, which generates the signal beam, TG. Because the sample is a monolayer, the grating is in the thin grating limit (Raman-Nath diffraction), so the probe beam can be brought in at any angle. The signal will emerge in the Bragg diffraction direction. Because a TG signal is well separated from the other beams, it can be overlapped with the external local oscillator for heterodyne detection that can amplify the signal.[33,44] Heterodyne detection results in the signal being at the E-field level ($E_{TG} \propto P^{(3)}(t)$), consistent with the results derived above. In the absence of heterodyne detection, the TG signal is at the intensity level ($|E_{TG}|^2$), and data analysis requires taking the absolute value squared of the results given above and the results given in this and Sec. V C on the BOXCARS geometry.

In the configuration in Figure 9(b), the k-vectors for all the input beams (B1, B2, and B3) and the signal beam (TG) are in the Y_LZ_L plane. The angle between the excitation beams (B1 and B2) is 2Φ, and the probe beam (B3) is the bisector of this angle (see Figure 9(b)). The polarization for the probe beam (B3) and the detection polarization for the TG signal is always set parallel to the X_L axis. In this configuration, each orientational response function is given by

$$R^{\chi=0^\circ}_{XXXX} = R^{\chi}_{XXXX} = \frac{1}{9} - \frac{4}{9}\sqrt{\frac{\pi}{5}}\langle Y_2^0\rangle + \frac{4}{45}\pi\langle Y_2^{0^*}Y_2^0\rangle + \frac{4}{15}\pi\langle Y_2^{2^*}Y_2^2\rangle, \quad (5.1)$$

$$R^{\chi=0^\circ}_{XXYY}(t) = \frac{1}{9}\cos 2\Phi - \frac{2}{9}\sqrt{\frac{\pi}{5}}\left(2\cos^2\Phi + \sin^2\Phi\right)\langle Y_2^0\rangle + \frac{4}{45}\pi\left(\cos^2\Phi + 2\sin^2\Phi\right)\langle Y_2^{0^*}Y_2^0\rangle - \frac{4}{15}\pi\cos^2\Phi\langle Y_2^{2^*}Y_2^2\rangle, \quad (5.2)$$

$$R^{\chi}_{XXYY} = \frac{1}{9}\cos 2\Phi - \frac{2}{9}\sqrt{\frac{\pi}{5}}\{2\cos(\chi+\Phi)\cos(\chi-\Phi) - \sin(\chi+\Phi)\sin(\chi-\Phi)\}\langle Y_2^0\rangle + \frac{4}{45}\pi\{\cos(\chi+\Phi)\cos(\chi-\Phi) - 2\sin(\chi+\Phi)\sin(\chi-\Phi)\}\langle Y_2^{0^*}Y_2^0\rangle - \frac{4}{15}\pi\cos(\chi+\Phi)\cos(\chi-\Phi)\langle Y_2^{2^*}Y_2^2\rangle. \quad (5.3)$$

See Section C of the supplementary material for the derivations.[36] Even though the actual functional forms of Eqs. (5.2) and (5.3) are different from Eqs. (2.22) and (2.31), the procedure for extracting the orientational correlation functions and population decay is the same. $\langle Y_2^0\rangle$ is determined by time averaged linear dichroism experiment, and then there are three equations with three unknown parameters, $\langle Y_2^{0^*}Y_2^0\rangle$, $\langle Y_2^{2^*}Y_2^2\rangle$, and $P(t)$. Thus all of these parameters can be obtained by solving Eqs. (5.1)–(5.3).

It is important to note that as shown in Eq. (5.1), $R^{\chi=0^\circ}_{XXXX} = R^{\chi}_{XXXX}$. This equality of two $XXXX$ signals is important for scaling the two signals with different χ angles as discussed in Sec. II C.

C. Heterodyne detected transient grating geometry with BOXCARS geometry

BOXCARS geometry for HDTG experiments can be very useful if, for example, 2D IR vibrational echo experiments are also conducted on the same sample using this beam geometry. In such a situation it is only necessary to change the timings of the pulses without any change in the beam geometry to perform the HDTG experiments.[33,44–46] In the BOXCARS geometry, beams are crossing both in the Y_LZ_L plane and in the X_LZ_L plane (see Figure 10(a)). The crossing of beams in both planes introduces substantial complexity in the observable response functions when the crossing angle is significant. "X" polarization for each beam is defined such that the polarization is in X_LZ_L plane and orthogonal to the propagation direction of the beam, whereas "Y" polarization is polarized in Y_LZ_L plane and normal to the k-vector of each beam. Beam B1 and B2 are the excitation beams that form the grating. Beam B3 is the probe, and TG is the transient grating signal that will be combined with the local oscillator for heterodyne

detection. The angle, Φ, is shown in Figure 10(a). The angles are relative to the dashed green line in Figure 10(a), which is perpendicular to the input plane and is equidistant from each of the input beams, B1, B2, and B3. For this configuration, orientational response functions can be written as

$$R^{\chi=0^\circ}_{XXXX} = \cos^2\Phi\left[\frac{1}{9} - \frac{4}{9}\sqrt{\frac{\pi}{5}}\left\langle Y_2^0\right\rangle + \frac{4}{45}\pi\left\langle Y_2^{0^*}Y_2^0\right\rangle + \frac{4}{15}\pi\left\langle Y_2^{2^*}Y_2^2\right\rangle\right] - \sin^2\Phi\left\{\frac{4}{15}\pi\left\langle Y_2^{1^*}Y_2^1\right\rangle\right\}, \tag{5.4}$$

$$R^{\chi=0^\circ}_{XXYY} = \cos^2\Phi\left[\frac{1}{9} - \frac{4}{9}\sqrt{\frac{\pi}{5}}\left\langle Y_2^0\right\rangle + \frac{4}{45}\pi\left\langle Y_2^{0^*}Y_2^0\right\rangle - \frac{4}{15}\pi\left\langle Y_2^{2^*}Y_2^2\right\rangle\right], \tag{5.5}$$

$$\begin{aligned} R^{\chi}_{XXXX} = {} & \cos^2\Phi\left[\frac{1}{9} - \frac{4}{9}\sqrt{\frac{\pi}{5}}\left\langle Y_2^0\right\rangle + \frac{4}{45}\pi\left\langle Y_2^{0^*}Y_2^0\right\rangle + \frac{4}{15}\pi\left\langle Y_2^{2^*}Y_2^2\right\rangle\right] \\ & - \sin^2\Phi\cos^2\chi\left\{\frac{4}{15}\pi\left\langle Y_2^{1^*}Y_2^1\right\rangle\right\} \\ & - \sin^2\Phi\sin^2\chi\left\{\frac{4}{15}\pi\left\langle Y_2^{2^*}Y_2^2\right\rangle\right\}, \end{aligned} \tag{5.6}$$

$$\begin{aligned} R^{\chi}_{XXYY} = {} & \frac{1}{9}\cos^2\Phi \\ & - \frac{2}{9}\sqrt{\frac{\pi}{5}}\{2\cos\Phi\cos(\chi+\Phi)\cos\chi \\ & - \cos\Phi\sin(\chi+\Phi)\sin\chi\}\left\langle Y_2^0\right\rangle \\ & + \frac{4\pi}{45}\{\cos\Phi\cos(\chi+\Phi)\cos\chi \\ & - 2\cos\Phi\sin(\chi+\Phi)\sin\chi\}\left\langle Y_2^{0^*}Y_2^0\right\rangle \\ & - \frac{4\pi}{15}\cos\Phi\cos(\chi+\Phi)\cos\chi\left\langle Y_2^{2^*}Y_2^2\right\rangle. \end{aligned} \tag{5.7}$$

Depending on the crossing angle Φ and the structure factor, implementation of this geometry presents two issues. First, in R^{χ}_{XXXX} (Eq. (5.4)), an additional spherical harmonic correlation function, $\langle Y_2^{1^*}Y_2^1\rangle$, appears. Second, R^{χ}_{XXXX} is not equal to $R^{\chi=0^\circ}_{XXXX}$, which can introduce an error when the R^{χ}_{XXYY} signal is scaled based on these two measurements. If the crossing angle is sufficiently small, both problems are negligible. As seen in Eq. (5.4), $\langle Y_2^{1^*}Y_2^1\rangle$ is multiplied by $\sin^2\Phi$, thus if Φ is small this term can be dropped. Also for small Φ, the scaling error becomes insignificant. For example, for an order parameter of −0.2 and $\Phi = 10^\circ$, the term with $\langle Y_2^{1^*}Y_2^1\rangle$ can be dropped and the scaling error is negligible. Ten degrees is actually a fairly large angle in an experiment. These issues are discussed in complete detail in Section C of the supplementary material.[36]

D. Fluorescence geometry

In a fluorescence experiment, the excitation beam impinges on the surface so that the X and Y polarizations coincide with X_L and Y_L axes in lab frame (see Figure 10(b)). That is, the k-vector of the excitation beam is the Z_L axis in the lab frame. The sample is again installed so that Z_S axis on the surface is perpendicular to X_L axis in lab frame. For $\chi \neq 0^\circ$ measurement, the sample is tilted in Y_LZ_L plane as shown in Figure 10(b). Upon excitation, a "cone" of fluorescence will be collected by a lens. The half-cone angle of the collected fluorescence is Θ. The fluorescence collimated by the lens passes through a polarizer to selectively detect X_L-polarized fluorescence, and the excitation beam polarization is rotated between X_L and Y_L.

The derivation and discussion of the following results are given in the supplementary material.[36]

$$\begin{aligned} R^{\chi=0^\circ}_{XXXX} = {} & \frac{1}{9} - \frac{2}{9}\sqrt{\frac{\pi}{5}}\{2I_1(\Theta) - I_2(\Theta)\}\left\langle Y_2^0\right\rangle \\ & + \frac{4}{45}\pi\{I_1(\Theta) - 2I_2(\Theta)\}\left\langle Y_2^{0^*}Y_2^0\right\rangle \\ & + \frac{4}{15}\pi I_1(\Theta)\left\langle Y_2^{2^*}Y_2^2\right\rangle, \end{aligned} \tag{5.8}$$

$$\begin{aligned} R^{\chi=0^\circ}_{XXYY} = {} & \frac{1}{9} - \frac{2}{9}\sqrt{\frac{\pi}{5}}\{2I_1(\Theta) - I_2(\Theta)\}\left\langle Y_2^0\right\rangle \\ & + \frac{4}{45}\pi\{I_1(\Theta) - 2I_2(\Theta)\}\left\langle Y_2^{0^*}Y_2^0\right\rangle \\ & - \frac{4}{15}\pi I_1(\Theta)\left\langle Y_2^{2^*}Y_2^2\right\rangle, \end{aligned} \tag{5.9}$$

$$\begin{aligned} R^{\chi=0^\circ}_{XXXX} = {} & \frac{1}{9} - \frac{2}{9}\sqrt{\frac{\pi}{5}}\{2I_1(\Theta) - (3\cos^2\chi - 2)I_2(\Theta)\}\left\langle Y_2^0\right\rangle \\ & + \frac{4}{45}\pi\{I_1(\Theta) - (3\cos^2\chi - 1)I_2(\Theta)\}\left\langle Y_2^{0^*}Y_2^0\right\rangle \\ & + \frac{4}{15}\pi\{I_1(\Theta) + \sin^2\chi\cdot I_2(\Theta)\}\left\langle Y_2^{2^*}Y_2^2\right\rangle, \end{aligned} \tag{5.10}$$

$$\begin{aligned} R^{\chi=0^\circ}_{XXYY} = {} & \frac{1}{9} - \frac{2}{9}\sqrt{\frac{\pi}{5}}\{I_1(\Theta)\cdot(3\cos^2\chi - 1) - I_2(\Theta)\}\left\langle Y_2^0\right\rangle \\ & + \frac{4}{45}\pi\{I_1(\Theta)\cdot(3\cos^2\chi - 2) - (3\cos^2\chi - 2) \\ & \cdot(3\cos^2\chi - 1)\cdot I_2(\Theta)\}\left\langle Y_2^{0^*}Y_2^0\right\rangle \\ & - \frac{4}{15}\pi\{I_1(\Theta) - \sin^2\chi\cdot I_2(\Theta)\}\cos^2\chi\left\langle Y_2^{2^*}Y_2^2\right\rangle, \end{aligned} \tag{5.11}$$

where $I_1(\Theta)$ and $I_2(\Theta)$ are the integrals given by

$$I_1(\Theta) \equiv \frac{1}{2\pi(1-\cos\Theta)}\int_0^\Theta d\theta\sin\theta \times \int_0^{2\pi} d\phi\frac{\cos^2\theta}{\cos^2\theta + \sin^2\theta\cos^2\phi}, \tag{5.12}$$

$$I_2(\Theta) \equiv \frac{1}{2\pi(1-\cos\Theta)} \int_0^{\Theta} d\theta \sin\theta \times \int_0^{2\pi} d\phi \frac{\sin^2\theta\cos^2\phi}{\cos^2\theta + \sin^2\theta\cos^2\phi}. \quad (5.13)$$

Note that $I_1(\Theta) + I_2(\Theta) = 1$ for any Θ, and also $I_1(0) = 1$ and $I_2(0) = 0$ for the small cone (small Θ) limit. $I_1(\Theta)$ and $I_2(\Theta)$ can be numerically evaluated. For example, in case $\Theta = 10^\circ$, $I_1(\Theta) = 0.99$ and $I_2(\Theta) = 0.01$, indicating that the effect of collection cone is minor and small-crossing angle limit is valid. In practice, a collection cone half angle of 10° is fairly large.

In addition, R^{χ}_{XXXX} is not rigorously equal to $R^{\chi=0^\circ}_{XXXX}$. As mentioned in the previous discussions, the equality of R^{χ}_{XXXX} and $R^{\chi=0^\circ}_{XXXX}$ is used to scale the amplitude of R^{χ}_{XXYY}. The collection cone angle must be set small enough so that the difference between R^{χ}_{XXXX} and $R^{\chi=0^\circ}_{XXXX}$ is negligible. A quantitative discussion on the maximum acceptable collection half-angle Θ is provided in the supplementary material.[36]

VI. CONCLUDING REMARKS

We have developed the theory necessary to extract detailed orientational dynamics and structural information for molecules bound to a planar two-dimensional surface from polarization-resolved third-order resonant spectroscopy. The theory was applied specifically to UV/Vis or IR polarization selective pump-probe experiments, UV/Vis or IR heterodyne detected transient grating experiments, and time resolved fluorescence orientational anisotropy measurements. The theory is also applicable to chromophores in uniaxial systems such as planar phospholipid bilayers or aligned uniaxial liquid crystals. The usual orientational anisotropy observable, $r(t)$ in Eq. (1.1) is not the correct observable to be measured for molecules bound to a planar surface. As discussed in Sec. II, the orientation dynamics and structural information are related to the spherical harmonics correlation functions $\langle Y_2^{0^*} Y_2^0\rangle$ and $\langle Y_2^{2^*} Y_2^2\rangle$, which correspond to out-of-plane motions and (mainly) in-plane motions, respectively. It is demonstrated that four measurements ($R^{\chi=0^\circ}_{XXXX}(t)$, $R^{\chi=0^\circ}_{XXYY}(t)$, $R^{\chi}_{XXYY}(t)$, and $\langle S\rangle$) are necessary to determine the orientational correlation functions and isotropic population decay $P(t)$. In practice, another measurement of $R^{\chi}_{XXXX}(t)$ is useful to obtain the necessary absolute amplitude of $R^{\chi}_{XXYY}(t)$ so that it can be used with $R^{\chi=0^\circ}_{XXXX}(t)$ and $R^{\chi=0^\circ}_{XXYY}(t)$ to extract the orientation dynamics and structural information.

The general theoretical results were applied to the wobbling-in-a-cone model, which describes molecular motions that are restricted to a limited range of angles (the cone). For molecules bound to a surface, the axis of the cone can be normal to the surface or tilted. As described in Sec. IV, the experimental measurements yield $\langle Y_2^{2^*} Y_2^2\rangle$ and $\langle Y_2^{0^*} Y_2^0\rangle$ which permit the determination of the cone half-angle θ_C and tilt angle θ_{tilt}, as well as the orientational diffusion constant, D. In the initial derivations, all of the results are obtained for the beams in the small crossing angle limit. In Sec. V, the equations are modified to provide the results necessary to perform experiments with beam geometries that occur in experiments.

The theory presented here is immediately applicable to fast dynamics of functionalized planar monolayers studied by HDTG spectroscopy, pump-probe experiments, and fluorescence depolarization. To apply the theory presented here for the fluorescence depolarization studies, the absorption transition dipole moment and the emission transition dipole moment must be the same. If the absorption and emission dipoles do not coincide, the theory would need to be modified to take the difference in two dipoles' orientations into account.

In Secs. III and IV the theory was applied to the wobbling-in-a-cone model. It is important, however, to emphasize that the proposed experimental procedures presented in Secs. II and V are valid regardless of the nature of the molecular motions. Thus, the in-plane and out-of-plane orientational correlation functions, $\langle Y_2^{2^*} Y_2^2\rangle$ and $\langle Y_2^{0^*} Y_2^0\rangle$, obtained from experiments can be compared with those obtained from molecular dynamics (MD) simulations. MD simulations of interfacial molecules have been presented.[47–52] As seen in Sec. IV, the essential features of interfacial molecular motions are captured in the correlation functions rather than each response function. Thus, the experiments proposed in this article, which directly obtain the correlation functions, should enable detailed comparison between experiment and MD simulations.

ACKNOWLEDGMENTS

This material is based upon work supported by the Air Force Office of Scientific Research Grant FA9550-12-1-0050. We thank Patrick Kramer and Amr Tamimi for useful discussions. Jun Nishida also thanks the Stanford Graduate Fellowship programs for graduate fellowships.

[1] A. Devadoss and C. E. D. Chidsey, J. Am. Chem. Soc. **129**, 5370 (2007).
[2] T. J. Terry and T. D. P. Stack, J. Am. Chem. Soc. **130**, 4945 (2008).
[3] D. G. Castner and B. D. Ratner, Surf. Sci. **500**, 28 (2002).
[4] K. Kinosita, Jr., S. Kawato, and A. Ikegami, Biophys. J. **20**, 289 (1977).
[5] G. Lipari and A. Szabo, Biophys. J. **30**, 489 (1980).
[6] C. C. Wang and R. Pecora, J. Chem. Phys. **72**, 5333 (1980).
[7] T. Tao, Biopolymers **8**, 609 (1969).
[8] S. Woutersen, U. Emmerichs, and H. J. Bakker, Science **278**, 658 (1997).
[9] R. S. Moog, M. D. Ediger, S. G. Boxer, and M. D. Fayer, J. Phys. Chem. **86**, 4694 (1982).
[10] A. Tokmakoff, J. Chem. Phys. **105**, 1 (1996).
[11] I. N. Ivanov, R. Dabestani, A. C. Buchanan, and M. E. Sigman, J. Phys. Chem. B **105**, 10308 (2001).
[12] M. E. Sigman, S. Read, J. T. Barbas, I. Ivanov, E. W. Hagaman, A. C. Buchanan, R. Dabestani, M. K. Kidder, and P. F. Britt, J. Phys. Chem. A **107**, 3450 (2003).
[13] S. Kawato, K. Kinosita, Jr., and A. Ikegami, Biochemistry **16**, 2319 (1977).
[14] D. E. Moilanen, E. E. Fenn, D. Wong, and M. D. Fayer, J. Chem. Phys. **131**, 014704 (2009).
[15] M. D. Fayer and N. E. Levinger, Annu. Rev. Anal. Chem. **3**, 89 (2010).
[16] A. Szabo, J. Chem. Phys. **81**, 150 (1984).
[17] B. W. Van der Meer, R. P. H. Kooyman, and Y. K. Levine, Chem. Phys. **66**, 39 (1982).
[18] R. P. H. Kooyman, M. H. Vos, and Y. K. Levine, Chem. Phys. **81**, 461 (1983).
[19] M. J. Van De Ven and Y. K. Levine, BBA-Biomembranes **777**, 283 (1984).
[20] F. Mulders, H. Van Langen, G. Van Ginkel, and Y. K. Levine, BBA-Biomembranes **859**, 209 (1986).
[21] G. Deinum, H. Van Langen, G. Van Ginkel, and Y. K. Levine, Biochemistry **27**, 852 (1988).
[22] Y. Zhang, M. A. Firestone, T. B. Rauchfuss, and P. W. Bohn, J. Phys. Chem. **100**, 13804 (1996).

[23]K. J. Rothschild and N. A. Clark, Biophys. J. **25**, 473 (1979).
[24]J. Umemura, T. Kamata, T. Kawai, and T. Takenaka, J. Phys. Chem. **94**, 62 (1990).
[25]S. Yamaguchi and T. Tahara, J. Chem. Phys. **129**, 101102 (2008).
[26]D. Zimdars, J. I. Dadap, K. B. Eisenthal, and T. F. Heinz, J. Phys. Chem. B **103**, 3425 (1999).
[27]X. Shang, K. Nguyen, Y. Rao, and K. B. Eisenthal, J. Phys. Chem. C **112**, 20375 (2008).
[28]C. S. Hsieh, R. K. Campen, A. C. V. Verde, P. Bolhuis, H. K. Nienhuys, and M. Bonn, Phys. Rev. Lett. **107**, 116102 (2011).
[29]H.-K. Nienhuys and M. Bonn, J. Phys. Chem. B **113**, 7564 (2009).
[30]M. J. Wirth and J. D. Burbage, Anal. Chem. **63**, 1311 (1991).
[31]M. J. Wirth and J. D. Burbage, J. Phys. Chem. **96**, 9022 (1992).
[32]S. Tsukahara, Y. Yamada, and H. Watarai, Langmuir **16**, 6787 (2000).
[33]J. Nishida, C. Yan, and M. D. Fayer, J. Phys. Chem. C **118**, 523 (2014).
[34]C. Zannoni, Mol. Phys. **38**, 1813 (1979).
[35]A. Szabo, J. Chem. Phys. **72**, 4620 (1980).
[36]See supplementary material at http://dx.doi.org/10.1063/1.4870436 for (A) proof of the orthogonality of the surface frame correlation function of the spherical harmonics; (B) derivations of the correlation functions of the spherical harmonics in the surface frame for wobbling-in-a-cone; and (C) derivations of the modifications of the response functions for beams with significant crossing angles and fluorescence with a substantial collection cone.
[37]S. Mukamel and R. F. Loring, J. Opt. Soc. Am. B **3**, 595 (1986).
[38]S. Mukamel, *Principles of Nonlinear Optical Spectroscopy* (Oxford University Press, New York, 1995).
[39]T. Joo, Y. Jia, J. Y. Yu, M. J. Lang, and G. R. Fleming, J. Chem. Phys. **104**, 6089 (1996).
[40]Z. Gengeliczki, D. E. Rosenfeld, and M. D. Fayer, J. Chem. Phys. **132**, 244703 (2010).
[41]D. E. Rosenfeld, J. Nishida, C. Yan, Z. Gengeliczki, B. J. Smith, and M. D. Fayer, J. Phys. Chem. C **116**, 23428 (2012).
[42]K. B. Eisenthal, Chem. Phys. Lett. **6**, 155 (1970).
[43]S. Woutersen and H. J. Bakker, Nature (London) **402**, 507 (1999).
[44]D. E. Rosenfeld, Z. Gengeliczki, B. J. Smith, T. D. P. Stack, and M. D. Fayer, Science **334**, 634 (2011).
[45]S. Park, K. Kwak, and M. D. Fayer, Laser Phys. Lett. **4**, 704 (2007).
[46]D. M. Jonas, Annu. Rev. Phys. Chem. **54**, 425 (2003).
[47]A. R. van Buuren, S. J. Marrink, and H. J. Berendsen, J. Phys. Chem. **97**, 9206 (1993).
[48]O. A. Karim and A. D. J. Haymet, J. Chem. Phys. **89**, 6889 (1988).
[49]S. A. Kislenko, I. S. Samoylov, and R. H. Amirov, Phys. Chem. Chem. Phys. **11**, 5584 (2009).
[50]Y. Nagata and S. Mukamel, J. Am. Chem. Soc. **132**, 6434 (2010).
[51]Y. Nagata and S. Mukamel, J. Am. Chem. Soc. **133**, 3276 (2011).
[52]Y. Nagata, C. S. Hsieh, T. Hasegawa, J. Voll, E. H. Backus, and M. Bonn, J. Phys. Chem. Lett. **4**, 1872 (2013).